LUND UNIVERSITY

Master Thesis

Investigation of Governing Physics in a PEM Electrolyzer

by

Kian Hajireza

Department of Chemical Engineering
Lund University
Sweden
December 21, 2020

Supervisor: **Doctor Niklas Andersson**
Examiner: **Professor Bernt Nilsson**
Assistant Supervisor: **Profesor Göran Lindbergh**

Postal address
PO-Box 124
SE-221 00 Lund,
Sweden
Web address
www.lth.se/chemeng

Visiting address
Naturvetarvägen 14

Telephone
+46 46-222 82 85
+46 46-222 00 00

Printed in Sweden by Media-Tryck.
Lund 2020

LUND UNIVERSITY

DEGREE PROJECT IN TECHNOLOGY,
SECOND CYCLE, 30 CREDITS
LUND, SWEDEN 2020

Investigation of Governing Physics in a PEM Electrolyzer

Master Thesis 2020

Kian Hajireza

LTH LUND UNIVERSITY
CHEMICAL ENGINEERING - DERPARTMENT OF CHEMICAL ENGINEERING

Author

Kian Hajireza ki5041ha-s@student.lu.se
Chemical Engineering

Place for Project

Stockholm, Sweden
KTH Royal Institute of Technology
Applied Electrochemistry Department

Examiner

Professor Bernt Nilsson
Lund
Faculty of Engineering (LTH)

Supervisor

Doctor Niklas Andersson
Lund
Faculty of Engineering (LTH)

Assistant Supervisor

Professor Göran Lindbergh [1]

PhD candidate Henrik Grimler [1]

Doctor Henrik Ekström [2,1]

Stockholm

[1]KTH Royal Institute of Technology, Teknikringen 42, SE-114 28 Stockholm, Sweden
[2]COMSOL AB, Tegnérgatan 23, SE-111 40 Stockholm, Sweden

Abstract

Hydrogen gas is an energy source that has an energy density (per mass) that is three times as large than the energy density of natural gas. This qualifies hydrogen gas as a prime candidate for the fuel of tomorrow. One of the main research areas for hydrogen include the production of it as there are a vast amount of methods of hydrogen production. Renewable hydrogen can potentially be produced through water electrolysis, which is investigated in this thesis.

The aim was to model and simulate the behaviour of a two—dimensional Polymer Electrolyte Membrane Electrolysis Cell (PEMEC) using COMSOL Multiphysics 5.5. Once the model was complete and compared with experimental data from the literature, the model was used to investigate the losses that take place in a PEMEC by considering five various cases with different assumptions made in each case. To take it one step further, a sensitivity analysis was performed to determine to what extent the parameters would affect the system efficiency.

In summary, the results showed that temperature contributed largely to the mass transport loss in the polarization curves. In general, the losses were larger for a higher temperature. Taking only the electrochemistry into account, resulted in the lowest loss at low current densities. Using a multi—phase model together with a water transport model yielded the largest loss at intermediate to high current densities, regardless of temperature. The sensitivity analysis showed that by doubling the catalyst layer thickness, a clear mass transport loss is visible, thus, showing that the catalyst layer thickness has a large effect on the model.

Sammanfattning

Vätgas är en energikälla som har en energidensitet (per massa) tre gånger så stor som naturgas. Detta gör så att vätgas är en huvudkandidat för morgondagens bränsle. Ett av de viktigaste forskningsområderna för vätgas innefattar produktion av vätgas eftersom det finns en stor mängd metoder för vätgasproduktion. Återvinnbar vätgas kan potentiellt produceras med vattenelektrolys, som undersöks i detta examensarbete.

Syftet var att modellera och simulera beteendet hos en tvådimensionell polymerelektrolytmembran elektrolytiskcell (PEMEC) med hjälp av COMSOL Multiphysics 5.5. När modellen var klar och den hade jämförts med experimentell data, användes modellen för att undersöka de förluster som sker i en PEMEC genom att studera fem olika fall med olika antaganden i varje fall. För att ta modellen ett steg vidare utfördes det en känslighetsanalys för att avgöra i vilken utsträckning parametrarna skulle påverka effektiviteten av systemet.

Sammantaget visade resultaten att temperaturen till stor del bidrog till en masstransportförlust i polarisationskurvorna. I allmänhet var förlusterna större för högre temperatur. Om man bara tar hänsyn till elektrokemin, resulterade det i den lägsta förlusten vid låga strömtätheter. Att använda en flerfasmodell tillsammans med en vattentransportmodell gav den största förlusten vid mellanliggande till höga strömtätheter, oavsett temperatur. Känslighetsanalysen visade att genom en fördubbling av katalysatorskikttjockleken är en tydlig masstransportförlust synlig, vilket visar att katalysatorskikttjockleken har stor effekt på modellen.

Populärvetenskaplig Sammanfattning

Vätgas är en viktig gas med många praktiska tillämpningar såsom bränsle i bränsleceller och som reduktionsmedel i den kemiska industrin. Just nu produceras vätgas vanligtvis med ångreformering. Ångreformering har nackdelen att den inte använder sig av hållbara reaktanter såsom metan och att den producerar koldioxid som biprodukter, som bidrar till växthuseffekten. En alternativ metod för att producera vätgas är elektrolys. Elektrolys använder sig endast av vatten och elektricitet som betraktas vara en hållbar energikälla beroende på vilken metod man använder för att producera elektricitet.

Polymerelektrolytmembran elektrolys cell (PEMEC) är en specifik typ metod för elektrolys som hittills inte studerats mycket. I detta arbete har därför detta system undersöks genom simuleringar, för att undersöka hur olika fysikaliska processer påverkar det. Ett simuleringsredskap som används för att genomföra simuleringen. När simuleringen är genomförd, analyseras och jämförs fem olika fall, där tas hänsyn till olika fysik och fenomen. Även en känslighetsanalys genomfördes för att se vilka parametrar som hade starkast påverkan på modellen.

Resultatet av denna insats var att förlusterna var större vid högre temperaturer. Känslighetsanalysen visade att en katalysatorparametrar hade starkast påverkan på modellen jämfört med de andra parametrar som analyserades. Med detta, transporten av kemiska specier visade sig ha mindre betydelse i systemet. Framtida arbete inkluderar att ta hänsyn till hydrofobiciteten av det material som brukar användas med annorlunda metoder.

Acknowledgements

To start with, I would like to thank Göran Lindbergh for giving me the opportunity of doing my master's thesis at the Applied Electrochemistry department. Additionally I would like to thank Henrik Grimler for tirelessly helping me through meetings and feedback. I would also like to thank Henrik Ekström for assisting with COMSOL support.

Lastly, a special thank you to my family for supporting me in the push to reach my dreams.

Acronyms

OER oxygen evolution reaction

HER hydrogen evolution reaction

PEM polymer electrolyte membrane

PEMEC Polymer Electrolyte Membrane Electrolysis Cell

VOF volume of fluid

GDL gas diffusion layers

CL catalyst layer

PDE partial differential equation

FEM Finite Element Method

MWR Method of Weighted Residuals

PEMFC Polymer Electrolyte Membrane Fuel Cell

OCV open circuit voltage

HP-PEMEC High-Pressure Polymer Electrolyte Membrane Electrolysis Cell

NSE Navier-Stokes equations

SOEC Solid oxide electrolysis cell

AEC Alkaline electrolysis cell

MEC Micriobial electrolysis cell

LMA Levenberg—Marquardt algorithm

FC flow channel

BP bipolar plate

Contents

1 Introduction **1**

1.1 Overview 1

1.2 Aim 2

1.3 Acknowledgement of Softwares 3

2 Theory **4**

2.1 Basics about electrolysis 4

2.2 Related Work 6

2.3 Electrochemical modelling 8

2.4 Transport of species 8

2.5 Multi—phase flow 9

3 Methods **11**

3.1 Workflow Process 11

3.2 Geometry and Mesh 12

3.3 The Finite Element Method 13

3.4 Modelling 15

3.4.1 Electrochemical Modelling 16

3.4.2 Species Transport 17

3.4.3 Darcy's Law for Multi—phase Flow 23

3.4.4 Boundary Conditions 25

3.4.5 General Assumptions 26

3.5 Cases 28

3.5.1 Case 1 — No Flow Physics 28

3.5.2 Case 2 — H_2O (l) fed cathode 28

3.5.3 Case 3 — Dry Hydrogen 29

3.5.4 Case 4 — Extended Water Transport Model with Liquid Equilibration 29

3.5.5 Case 5 — Extended Water Transport Model with Simultaneous Liquid Equilibration and Vapor Equilibration in the Cathode . . . 30
3.6 Final Remarks . . . 30

4 Results and Discussion **32**
4.1 Comparison of Cases . . . 32
4.2 Sensitivity Analysis . . . 36
4.3 Model Verification . . . 38

5 Conclusion **43**
5.1 Limitations . . . 43
5.2 Future Work . . . 44
5.3 Final Words . . . 44

6 Bibliography **52**

A Additional Results **57**

B Extended Water Transport Model **59**

C Parameters **61**

D Material properties **63**

Chapter 1

Introduction

1.1 Overview

Hydrogen gas has many physical applications such as in fuel cells, in the chemical industry and it is also an important energy carrier in a future where energy production is green. Green in this context is defined as renewable and does not directly contribute to the greenhouse effect. Due to the growing importance of fuel cells and the applications of hydrogen in the chemical industry, this has caused the scientific community to become more invested in producing hydrogen gas. A list of options for methods of hydrogen production is shown in figure 1.1. Industrial production of hydrogen today commonly uses fossil fuels (methane), which reacts with steam to form carbon monoxide, carbon dioxide and hydrogen in a process called steam reforming. For a sustainable future, this method works against the two main objectives of a sustainable future. Firstly, the fact that this method produces carbon dioxide, which then contributes to climate change and secondly, the fact that it is not a renewable source of energy, it uses fossil fuel, which is only available for a finite amount. Steam reforming can also use biogas instead of fossil fuels, solving the renewability issue. Nevertheless, with this method, inadequate amounts of biogas are available for large-scale hydrogen usage. [Kumar and Himabundu, 2019]

Thus, an alternative method to produce hydrogen is necessary. One alternative method is the PEMEC, which is the focus of this thesis. Electrolysis unfortunately fulfills only one of the requirements of a green energy production, the fact that it does not contribute to the greenhouse effect. It uses water and electricity as its source,

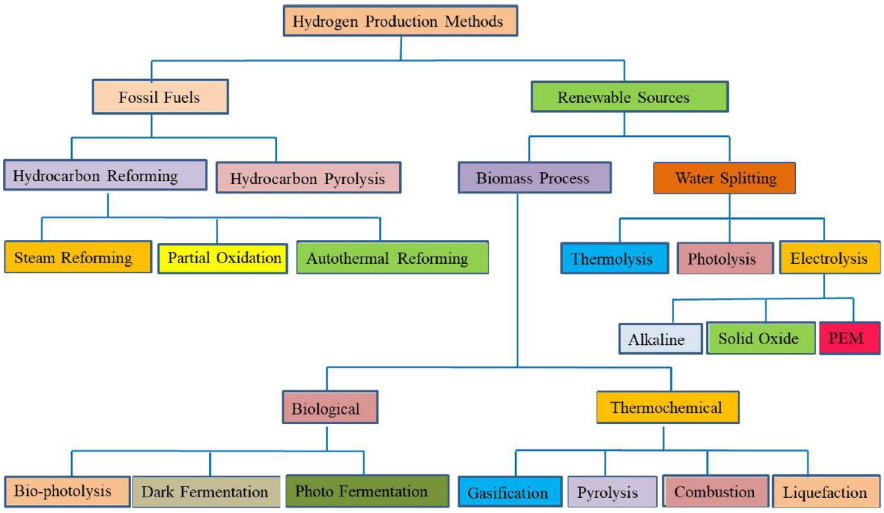

Figure 1.1: Different methods for hydrogen production [Kumar and Himabundu, 2019]

which are considered as both renewable and non—renewable resources, depending on the method used to produce the electricity.

As figure 1.1 shows, there are many production methods of hydrogen. The focus of this thesis will be on electrolysis with an acidic nafion membrane, a polymer electrolyte membrane (PEM).

1.2 Aim

The main aim of this project is to use a simulation tool such as COMSOL Multiphysics 5.5 to simulate the behaviour of a PEMEC in a two—dimensional numerical model. Once a successful model is created, the most important phenomena taking place in a PEMEC are investigated. Thereafter the model is used to explore and investigate which parameters and assumptions have the largest effect on the numerical model.

Delimitations of this project include:

- A two—dimensional model
- A single cell of a few squared centimeters is modelled. Thus, to clarify, the simulation is not of a stack of fuel cells.
- The model is steady—state.

For a more comprehensive and detailed review of the delimitations and assumptions

the reader is referred to section 3.4.5 General Assumptions.

1.3 Acknowledgement of Softwares

To perform this thesis, various softwares were in use such as COMSOL Multiphysics 5.5 for pre—processing, Python 3.9 for post–processing and lastly, Plot Digitizer 2.6.9 for data extraction.

Chapter 2

Theory

2.1 Basics about electrolysis

The term electrolysis originates from Greek and it is defined as the dissolution of electrons. Electrolytic reactions are non—spontaneous due to their positive Gibbs free energy, this implies that an external force must be applied for the reaction to occur, which implies that external energy is required. For electrolytic cells this corresponds to the application of a cell voltage. A galvanic reaction is the reverse reaction that occurs spontaneously in a galvanic cell [P. Atkins and Laverman, 2016]. There are various forms of electrolysis that can be used to produce hydrogen, such as PEMECs, Solid oxide electrolysis cell (SOEC)s, Alkaline electrolysis cell (AEC)s, Micriobial electrolysis cell (MEC)s, among many others. The focus of this thesis will be solely on PEMEC and the other techniques are not explained, instead the reader is encouraged to read Kumar and Himabundu [2019] for more information regarding the other techniques mentioned.

Figure 2.1 shows the operation of a PEMEC. The anode is known as the O_2 side and the cathode is known as the H_2 side. As it is illustrated in the figure, water enters the anode and produces oxygen bubbles, with the reaction shown below happening in the catalyst layer (CL). This reaction is called the oxygen evolution reaction (OER).

$$2\,H_2O \longrightarrow 4\,H^+ + 4\,e^- + O_2$$

The protons that are produced in the reaction above, are transported through the semipermeable Nafion membrane to the cathode. The electrons travel through an

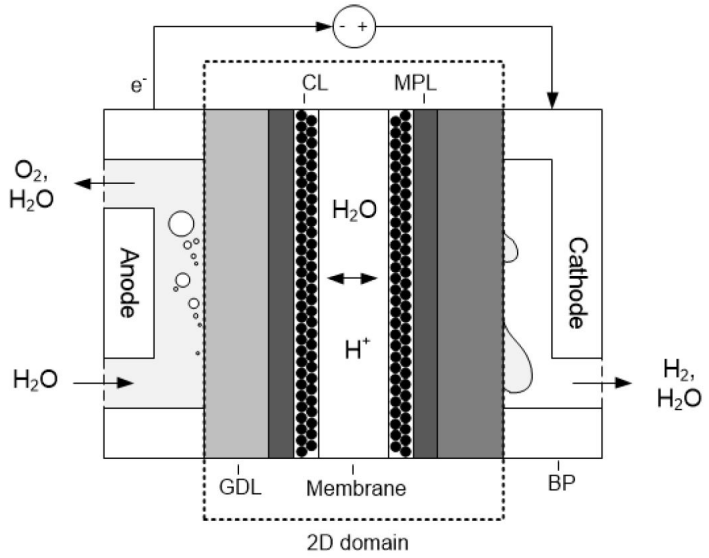

Figure 2.1: Illustration of a polymer electrolyte membrane electrolytic cell when liquid water is present only in the anode and water vapour in the cathode. [Olesen and Kær, 2015]

external circuit, arriving to the cathode, where the electrons reduce the protons to form hydrogen gas, as the reaction below shows. This reaction is called the hydrogen evolution reaction (HER).

$$4\,H^+ + 4\,e^- \longrightarrow 2\,H_2$$

Figure 2.2 illustrates the general appearance of a polarization curve for an electrolyzer. The overall performance,V_{cell}, represented by the blue curve, is the sum of all of the given losses and the equilibrium electrode potential as shown in equation 2.1, where E_{eq} is the equilibrium electrode potential, η_{Act} is the voltage activation loss, η_{Diff} is the voltage loss responsible by mass transfer and lastly, η_{Ohm} is the ohmic loss.

$$V_{\text{cell}} = E_{eq} + V_{\text{Act}} + V_{\text{Diff}} + V_{\text{Ohm}} \tag{2.1}$$

As the figure shows, the activation loss is logarithmic and contributes mostly to the shape of the cell performance curve at low current densities. The activation loss occurs due to that some voltage is forfeited for the half—cell reactions to take place, in other words to activate the reactions. Figure 2.2 also shows a linear trend for ohmic losses, which are due to resistances in charge transport. Finally, the mass transfer

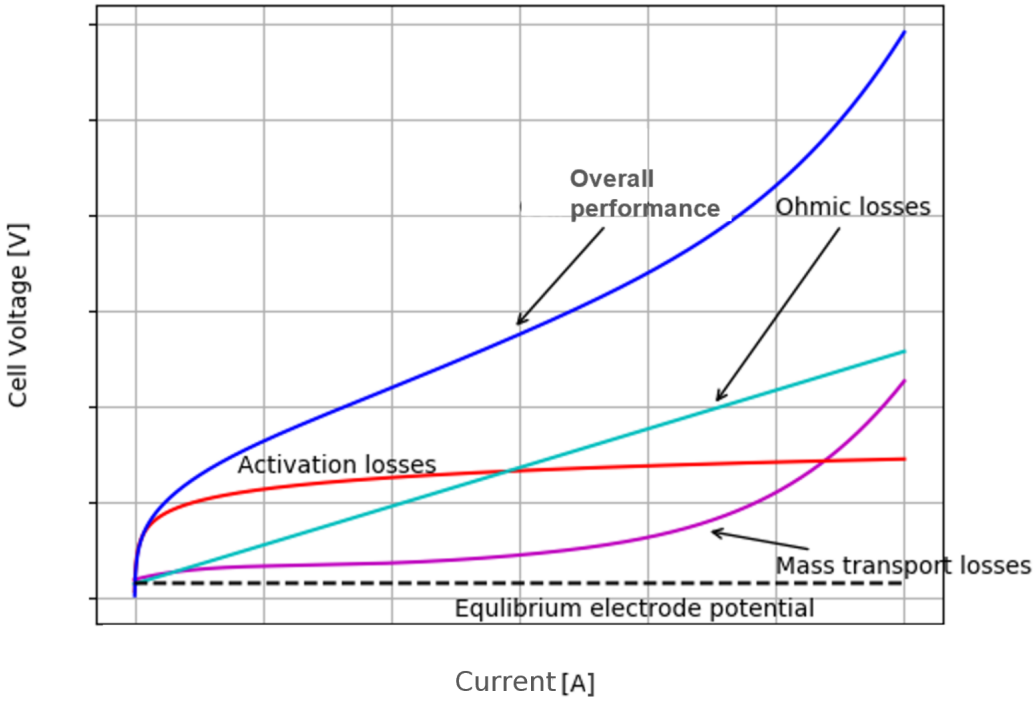

Figure 2.2: An illustration of a polarization curve with its contributing factors.

losses occur at high current densities and are due to large reactant concentrations, which reduce the rate of reaction due to molecules blocking the active sites [Biaku et al., 2008].

2.2 Related Work

There has been substantially more work on Polymer Electrolyte Membrane Fuel Cell (PEMFC) than PEMEC. With one of the first PEMEC models originating as late as 2002. [Onda et al., 2002] Thus, it is a relatively new area of research, which needs expanding.

The existing models are composed of different levels of complexity and model dimensions. For example in Han et al. [2015], a zero—dimensional model at steady—state was constructed. The individual voltage losses modelled as shown in equation 2.2. Each loss component was then composed of algebraic expressions. Where the open circuit voltage (OCV), E_{OCV} and the diffusion overpotential, η_{Diff} were calculated using Nernst equation. The activation overpotential, η_{Act} was modelled with the Butler—Volmer equation and lastly, the ohmic overpotential, η_{Ohm} was modelled with Ohm's law. The simulation studied to what extent certain design

parameters would affect the voltage losses with respect to current density. The design parameters that were varied were temperature, exchange current density (both anode and cathode), pressure, electrode thickness, membrane thickness and finally, the interfacial resistance. The results indicate that an increase in exchange current density and temperature and a decrease in pressure, electrode thickness, membrane thickness yield in lower voltage losses for a given current density.

$$\mathrm{E} = \mathrm{E_{OCV}} + \eta_{Act} + \eta_{Diff} + \eta_{Ohm} \tag{2.2}$$

Kim et al. [2012] created a one—dimensional model for a High-Pressure Polymer Electrolyte Membrane Electrolysis Cell (HP-PEMEC). The model consisted of unsteady mass and energy balances, meanwhile, the velocity was modelled at steady—state. The presented results showed that at decreasing pressures and current density, the system efficiency, increases. The reason behind this is that at larger current densities the voltage losses increase, which lowers the cell performance.

In Toghyani et al. [2018] a three—dimensional simulation of a bipolar plate is performed. The main purpose of this article was to investigate the flow pattern effects in the PEM electrolyzer. The study performed also used a steady—state condition. The flow was modelled with a form of the momentum equation, taking into account the porosity. The charge equation was used to model the electric potential, energy equation for the temperature and lastly, a species conservation to model the concentration. The simulation results were validated with experimental results but differed somewhat at high current densities. The presented results show a decrease in hydrogen concentration along the channel due to pressure drop and less availability of water since it is consumed. Interestingly, given the way the geometry is built, stagnation points are present. In these stagnation points, there are no electrochemical reactions present, leading to a decrease in hydrogen concentration (close to zero). The temperature profiles were larger at the inlet due to the vast presence of water and electrochemical reactions. Due to that the PEMEC reaction is exothermic once the cell voltage exceeds 1.48 V, the temperature increased along the channel.

2.3 Electrochemical modelling

The electrochemical model is constituted of a charge balance, which includes a source term from the electrochemical reactions. This can be accounted for by using the extended Butler—Volmer equation, shown in equation 2.3, which relates the current density, j_{v} to the overpotential, η. F is Faraday's constant, R is the universal gas constant, T is temperature and j_{0} is the exchange current density. $c_{\mathrm{o,s}}(x, y)$ is the surface concentration on the side where oxidation occurs, with $c_{\mathrm{r,s}}(x, y)$ being the surface concentration on the side where reduction occurs, c_{o}^{*} and c_{r}^{*} are reference concentrations on the oxidation side and the reduction side, respectively and a_{v} is the specific catalyst surface area.

α is the charge transfer coefficient. In many scientific articles within electrochemistry, this value is often assumed such as in Nie et al. [2009]. However, there have been attempts to determine this value, for example in Touré et al. [2018], the authors used an optimization technique to determine the charge transfer coefficient.

$$j_v = j_0 a_v \left\{ \frac{c_{o,s}(x,y)}{c_o^*} \exp\left[\frac{\alpha_{\mathrm{a}} z F \eta}{RT}\right] - \frac{c_{\mathrm{r,s}}(x,y)}{c_{\mathrm{r}}^*} \exp\left[-\frac{\alpha_{\mathrm{c}} z F \eta}{RT}\right] \right\} \tag{2.3}$$

2.4 Transport of species

In Weber and Newman [2004a], a mathematical model is presented and validated in Weber and Newman [2004b] in a fuel cell model, describing vapor—equilibrated and liquid—equilibrated transport in PEM, in which the transport of water across membrane is modelled. For a PEMEC the water is pumped into the cell through water channels, in which the water is in liquid phase. In the cathode, the hydrogen is not fully saturated and the membrane is moist, leading to the water evaporating, thus, on the cathode, the vapor—equilibrated transport should be taken into account. In the cathode, hydrogen gas is produced, and water is evaporated from the membrane phase, resulting in humidified gas. When there are two forms of equilibration present, the governing equations become equations B.1 and B.2. In this section solely the liquid—equilibration is presented and the simultaneous vapor— and liquid—equilibration is presented in Appendix B Extended Water Transport Model due to that simplifications of the simultaneous vapor and liquid transport were made in this thesis presented in 3.5.5 Case 5 — Extended Water Transport Model

with Simultaneous Liquid Equilibration and Vapor Equilibration in the Cathode. The equations used for liquid—equilibrated transport are 2.4 and 2.5. κ_{L} is the electrolyte conductivity for liquid—equilibrated transport, ξ_{L} is the electroosmotic drag coefficient for liquid—equilibrated transport and α_{L} is the transport coefficient for liquid—equilibrated transport. These variables are described more in detail in section 3.4.2 Extended Water Transport Model. μ_0 is the chemical potential of water, ϕ_l is the electrolyte potential and N_0 is the flux of water.

$$j_v = -\kappa_{\mathrm{L}} \nabla \Phi_l - \frac{\kappa_{\mathrm{L}} \xi_{\mathrm{L}}}{F} \nabla \mu_0 \tag{2.4}$$

$$N_0 = -\frac{\kappa_{\mathrm{L}} \xi_{\mathrm{L}}}{F} \nabla \Phi_l - \left(\alpha_{\mathrm{L}} + \frac{\kappa_{\mathrm{L}} \xi_{\mathrm{L}}^2}{F^2} \right) \nabla \mu_0 \tag{2.5}$$

2.5 Multi—phase flow

The flow is multi—phase, with liquid and gaseous states present. To model this multi—phase flow there are various methods such as volume of fluid (VOF)[Lafmejani et al., 2017, Niu et al., 2015], mixture model [Nie and Chen, 2009], extended Darcy's law [Berning et al., 2009] and lastly, bubbly flow [Larimi et al., 2018].

All of the mentioned methods above come with their benefits and disadvantages. The simplest multi—phase flow method of the above—mentioned is the extended Darcy's law, which likely helps simplifying the simulation but may not result in as accurate results as the others.

Darcy's law is an approximation of the Navier-Stokes equations (NSE). For Darcy's law it is assumed that there is no acceleration of the fluid present. This causes the material derivative, shown in equation 2.6 to be zero [Deen, 2012].

$$\frac{\mathrm{D}\mathbf{u}}{\mathrm{D}t} = \frac{\partial \mathbf{u}}{\partial t} + \mathbf{u} \cdot \nabla \mathbf{u} = 0 \tag{2.6}$$

$$\begin{aligned} \nabla \cdot (\rho \mathbf{u}) &= Q_m \\ \mathbf{u} &= -\tfrac{\kappa}{\mu} \nabla p \end{aligned} \tag{2.7}$$

This takes the NSE and turns it into a linear equation known as Darcy's law, shown in

equation 2.7, in combination with the continuity equation, where **u** is the velocity vector, t is time, ρ is density, Q_{m} is the mass source, κ is the permeability, μ is the dynamic viscosity and lastly, p is the pressure.

VOF is another method for taking multiphase flow into account as mentioned in the paragraphs above. VOF monitors a liquid—gas interface. VOF is a hyperbolic partial differential equation (PDE), where the volume fraction is the dependent variable. When using VOF, it needs to be coupled with NSE. The calculated volume fractions are used to calculate the viscosity and the density, which are later used in the NSE. This method does however not exist as a physics interface in COMSOL, nevertheless, it should not not be a hinder due to that with the help of PDE interfaces this hinder can be solved. With PDE interfaces any given PDE can be expressed. This method is fairly simplified to take into account for the multiphase flow part. Given that this method requires the coupling to the NSE, it will require a fair amount of computing power. [Lafmejani et al., 2017]

The mixture model is also used in combination with the NSE. A mass balance is formulated to solve for the volume fraction of the bubbles or droplets, which are later used in the continuity equation. To repeat the final part of the previous paragraph, to use this method, requires using the NSE, which will once again require considerable amount of computing power. This method was used in Nie and Chen [2009].

An additional method for taking into account the multi-phase flow is using the bubbly flow method. A variant of this is used in Larimi et al. [2018]. This also involves using the NSE. The NSE is used to solve for the velocity of the liquid phase and with the help of a slip model, the velocity of the dispersed bubbles is solved for using a slip model. Using a transport equation, the volume fractions can be solved for, which are later used in the continuity equation.

Considering the different methods presented in this section, Darcy's law for multi—phase flow was used to account for the multi—phase flow.

Chapter 3

Methods

3.1 Workflow Process

Figure 3.1 shows the workflow for this thesis. The first step according to the figure is to create the geometry. Once the geometry was constructed, the following step was to create a mesh for the geometry, dividing the geometry into small domains, where the governing equations are solved.

Once the mesh is complete, the physics of the model can be defined. The physics that are taken into account depend on the length and time scale of the model. There are also assumptions that are necessary to make to simplify the model complexity as all processes are not possible to take into account due to limited computational power. Appropriate boundary conditions are set that match the physical system and make the system of PDEs solveable. More information regarding the model can be found in

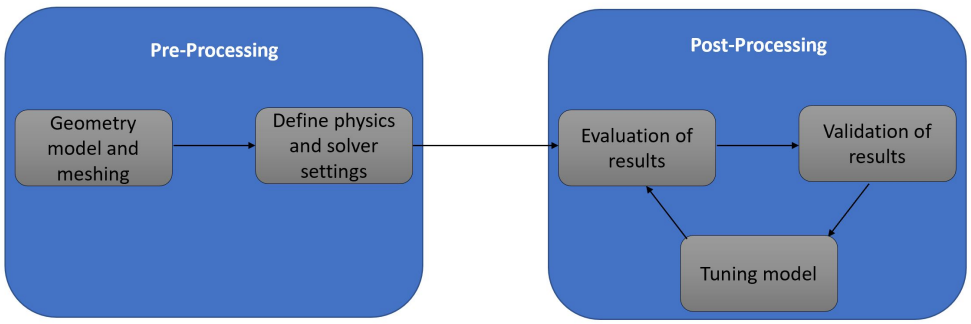

Figure 3.1: Workflow for model development divided into pre—processing and post—processing

section 3.4. The two steps mentioned are a subset of pre—processing.

The consecutive step is the post—processing as shown in figure 3.1. This is the most significant portion of a simulation, as in this part of the simulation workflow it can be deduced whether the results are reliable and plausible. This is done by analyzing surface plots and vector fields of relevant variables. The next two steps in figure 3.1 are closely related. The validation occurs by calibrating the model using the Levenberg—Marquardt algorithm (LMA) to tune parameters such as ionic conductivities, charge transfer coefficients and exchange current densities. The validation is done by comparing the polarization curve generated from the simulation with experimentally generated polarization curves. From this, the parameters can be estimated, in which the results need to reevaluated as figure 3.1 shows.

3.2 Geometry and Mesh

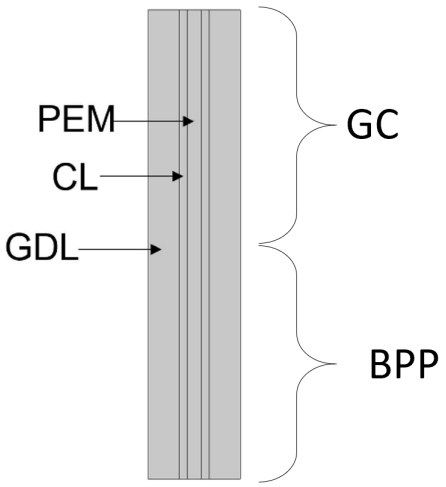

Figure 3.2: Geometry studied with the different domains marked

Figure 3.2 shows the geometry used for the simulations. It consists of two gas diffusion layers (GDL), two CLs and a PEM. The flow channel (FC) and the bipolar plate (BP) did not have any physics defined in them. The top half of the GDL is bounded by the FC and the lower half of the GDL is bounded by the BP.

Figure 3.3 shows the division of the different domains of the geometry, such as the GDL, CL and PEM. The geometry is fairly simple, consisting of rectangular blocks. Thus, a Cartesian grid was used shown in figure 3.3, specifically, a block-structured grid was utilized. This is characterized by the different domains in the figure having

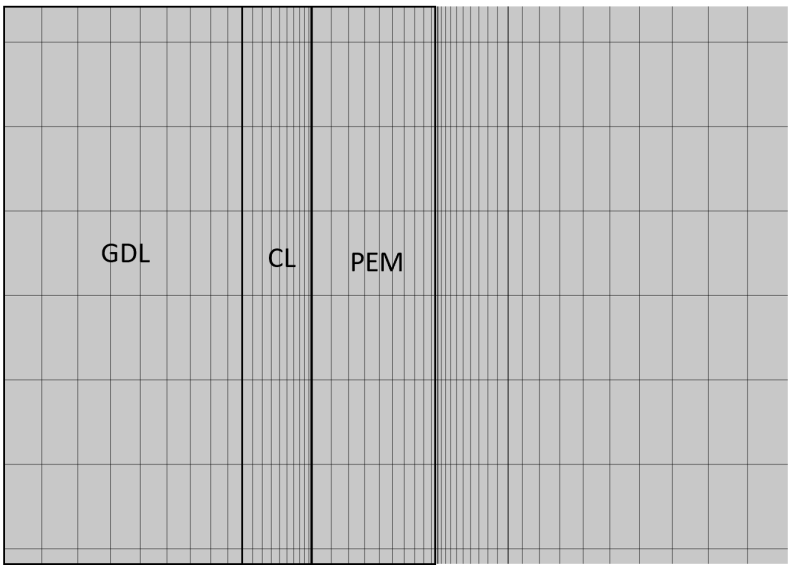

Figure 3.3: A zoomed in snapshot of the mesh of the geometry with the different regions of the PEM presented explicitly in the anode. The cathode also consists of the domains shown for the anode.

contrasting mesh structures. For the CL, the mesh is the finest domain as shown. This is due to that the electrochemical reactions occur in this region and thus, a finer mesh is required. As a matter of fact, the fineness of the mesh for the CL increases closer towards the PEM. This is due to that the electrochemical reactions occur very close to the PEM. Thus, to capture this effect, the element sizes were very small near the CL/PEM—interface. In addition, the fineness of the mesh for the PEM region increases closer to the cathode. After running a simulation, it became apparent that the current distribution was irregular due to that the overpotential, η was very small. To ensure that the simulated results are a valid solution, a mesh independence test was performed, meaning that the overall fineness of the mesh was increased until the results did not alter. [Versteeg and Malalasekera, 2007]

3.3 The Finite Element Method

To be able to solve the systems of PDEs numerically, the Finite Element Method (FEM) is used to discretize the equations. FEM is the numerical method used in COMSOL Multiphysics. FEM is divided into six different steps. The following concise description of the algorithm is for steady—state problems. The first step is to approximate the solution with the use of a basis function, which is often a piece—wise polynomial function. Figure 3.4 gives an illustration of FEM. $y(x)$ is the actual

solution, $u(x)$ is the approximated solution, a_j is the scaling factor and lastly, $\phi(x)$ is the basis function, which is usually a hat function as shown in figure 3.4. Equation 3.1 shows that a function $u(x)$ is used to mimic the behaviour of the actual function, $y(x)$, by adding the different basis functions multiplied with its respective scaling factor. [Nilsson, 2018]

$$y(x) \approx u(x) = \sum_{j=1}^{m} a_j \phi_j(x) \tag{3.1}$$

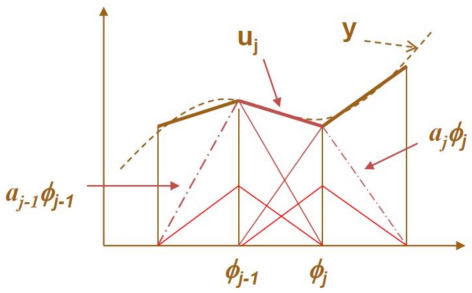

Figure 3.4: Graphical illustration of the finite element method [Nilsson, 2018]

The following step is to divide the geometry into small finite elements, which is done by creating a mesh. There are different element sizes that can be chosen. The smaller the element size, implies a finer mesh, which will give more accurate results however, take a longer time to converge, while the opposite is true for a coarser mesh. The problem size (number of variables), denoted as s in equation 3.2 depends on the order of basis P, number of dimensions Y, number of mesh elements B and the number of domain equations M.[Nilsson, 2018, Ottosen and Petersson, 1992]

$$s = PYBM \tag{3.2}$$

The third step is the finite element approximation, which is done with equations 3.3 and 3.4.

$$\frac{\partial y}{\partial x} \approx \frac{\partial u}{\partial x} = \sum_{j=1}^{m} a_j \frac{\partial \phi_j}{\partial x} \tag{3.3}$$

$$\frac{\partial^2 y}{\partial x^2} \approx \frac{\partial^2 u}{\partial x^2} = \sum_{j=1}^{m} a_j \frac{\partial^2 \phi_j}{\partial x^2} \tag{3.4}$$

The fourth step is to use the Method of Weighted Residuals (MWR), by setting a residual variable, e, equal to the discretized equation, this is known as the residual equation (also known as error function). The residual equation is multiplied by a weighting function. Using the Galerkin method to the set—up the equations, the weight function with this method is coincidentally, the basis function. The Galerkin method is used to convert a continuous problem into a discrete one. For more information about it, the reader is referred to a finite element method book such as Ottosen and Petersson [1992]. The integral of the residual equation multiplied with the basis is forced to be zero, as shown in equation 3.5.

The final step is to assemble the equations and solve the mean—weighted residual integrals. With this information, the sixth and final step is to determine the scaling coefficients, a. [Nilsson, 2018, Ottosen and Petersson, 1992]

$$\int_0^L \phi(x) R(x) dx = 0 \tag{3.5}$$

With the use of FEM, there are two contrasting representations of PDEs. They are called the strong form and the weak form. The difference is that the strong form is a representation of the conventional differential equation, whereas the weak form has its boundary conditions incorporated into the equations. The weak form has less constraints for differentiability and continuity. The strong form requires its basis functions to be differentiable twice, however the weak form requires the basis to only be differentiable once. The solution is required to be continuous for the strong form. Given all of the mentioned requirements, all solutions for the strong form are solutions for the weak form. [Nilsson, 2018, Ottosen and Petersson, 1992]

3.4 Modelling

This section presents the different equations, boundary conditions and assumptions used to model the PEMEC.

3.4.1 Electrochemical Modelling

The electrochemical model is built upon charge balances as shown in equation 3.6 and 3.7. Where Φ_{l} is the electrolyte potential and Φ_{s} is the metallic conductor potential, . They are computed by calculating the divergence of the current for its respective phase. σ_{l} and σ_{s} represent the electrolyte conductivity and the electrical conductivity, respectively.

$$-\nabla \cdot (\sigma_l \nabla \Phi_l) = 0 \tag{3.6}$$

$$-\nabla \cdot (\sigma_s \nabla \Phi_s) = 0 \tag{3.7}$$

The ionic conductivity, σ_{l} was modelled as a function of temperature and water content as shown in equation 3.8, which was empirically determined in Zawodzinski and Gottesfeld [1991]. σ_{s} is a constant.

$$\sigma_l = (0.005139\lambda - 0.00326) \exp\left[1268\left(\frac{1}{T_{\mathrm{ref}}} - \frac{1}{T}\right)\right] \tag{3.8}$$

λ is the water content, defined as the number of moles of water per mole of sulfonic acid sites in Weber and Newman [2004a] and T is temperature. T_{ref} is the reference temperature taken to be equal to room temperature.

Equation 3.6 is valid in the PEM and a version of the equation is valid in the CL. Equation 3.7 is valid in the GDL and a version of the equation is valid in CL. To clarify the equations used in the CL, the only difference between equations 3.6 and 3.7 and the equations that were actually used in the CL are that a total source term is used from the electrochemical reactions, $i_{\mathrm{v,tot}}$ and effective conductivities, $\sigma_{\mathrm{s,eff}}$ $\sigma_{\mathrm{l,eff}}$ are used as presented in equations 3.9 and 3.10.

$$-\nabla \cdot (\sigma_{l,eff} \nabla \Phi_l) = j_{v,tot} \tag{3.9}$$

$$-\nabla \cdot (\sigma_{s,eff} \nabla \Phi_s) = -j_{v,tot} \tag{3.10}$$

To account for that only a certain fraction of the catalyst layers consists of ionomer that can be used for ionic or electronic transport, effective conductivities are calculated through the Bruggeman relation shown in equations 3.11 and 3.12. Where ϵ_{l} is the electrolyte volume fraction and ϵ_{s} is the electrode volume fraction.

$$\sigma_{l,eff} = \epsilon_l^{1.5}\sigma_l \tag{3.11}$$

$$\sigma_{s,eff} = \epsilon_s^{1.5}\sigma_s \tag{3.12}$$

To calculate the total current source from the electrochemical reactions, the Butler—Volmer equation is used shown in equation 2.3, calculating it concentration *independent* by setting the reference concentration equal to its respective surface concentration. The exchange current densities, j_0, were taken to be temperature dependent using an Arrhenius equation. The cathodic exchange current density could be calculated using values from Durst et al. [2015] and the anodic current density could be calculated using values from Barbir [2005]. The general appearance of the equation is shown in equation 3.13.

$$j_0 = j_{0,ref} \exp\left[-\frac{\mathrm{E_a}}{\mathrm{RT}}\left(1 - \frac{\mathrm{T}}{\mathrm{T_{ref}}}\right)\right] \tag{3.13}$$

Where E_{a} is the activation energy, R is the universal gas constant and $j_{\mathrm{o,ref}}$ is the reference exchange current density at the reference temperature. The corresponding equation is used for the cathode.

3.4.2 Species Transport

This section will present the methods used to model the species transport. There are three different methods and techniques used to account for the species transport. One of the methods used were the Maxwell-Stefan equations for multicomponent gas diffusion. This was used to model the transport of water vapor together with hydrogen gas in the cathode. An additional method used was a mass balance, taking into account for the multi—phase flow, calculating the volume fractions, named phase transport in porous media. Lastly, an extended water transport model was used to take into account the water transport through the membrane.

Maxwell—Stefan equations

The Maxwell—Stefan describe multi—component diffusion and is used in the cathode when dealing with water vapor together with hydrogen gas. The equations are quite complex however they give a very accurate description of the diffusion. The Maxwell—Stefan equations are presented in equation 3.14, which is used to calculate the mass fraction, ω_{i}. J_{i} is the flux of specie i, u_{i} is the velocity of specie i, ρ is the density and lastly, R_{i} is the reaction term. [Bird et al., 2007]

$$\rho(\mathbf{u_i} \cdot \nabla)\omega_i = \nabla \cdot \mathbf{J_i} + R_i \tag{3.14}$$

The flux is then calculated in equation 3.15. Due to that there are only two components in the cathode, namely water vapor and hydrogen gas, the summation factor consists of only two components. d_{k} is the diffusional driving force that acts on specie, k.

$$\mathbf{J_i} = \rho\omega_i \sum_{k=1}^{2} \tilde{D}_{\mathrm{i,k}}\mathbf{d}_k \tag{3.15}$$

$$\tilde{D}_{\mathrm{i,k}} = D_{\mathrm{i,k}}\epsilon_p^{1/2} \tag{3.16}$$

$D_{\mathrm{i,\,k}}$ is the the multi-component diffusion coefficient. This was modelled as being both pressure and temperature dependent according to equation 3.17 [Bird, 1958]. With equation 3.16, the effective diffusivity can be calculated using a Bruggeman relationship.

$$D_{\mathrm{i,k}} = \frac{3.6410^{-4}}{p} \cdot \left(\frac{T}{\sqrt{T_{\mathrm{c,i}}T_{\mathrm{c,k}}}}\right)^{2.334} \left(p_{\mathrm{c,i}}p_{\mathrm{c,k}}\right)^{1/3} \left(T_{\mathrm{c,i}}T_{\mathrm{c,k}}\right)^{5/12} \left(\frac{1}{M_{\mathrm{i}}} + \frac{1}{M_{\mathrm{k}}}\right)^{1/2} \tag{3.17}$$

Where p is the absolute pressure, which is calculated in Darcy's law, $T_{\mathrm{c,i}}$ and $T_{\mathrm{c,k}}$ are the critical temperatures of specie i and k, respectively. $p_{\mathrm{c,i}}$ and $p_{\mathrm{c,k}}$ are the critical pressures of specie i and k, respectively and M_{i} and M_{k} are the molar masses of specie i and k, respectively.

Equation 3.18 shows the expression used for the diffusional driving force.

$$\mathbf{d}_k = \nabla x_k + \frac{1}{p}\left[(x_k - \omega_k)\,\nabla p\right] \tag{3.18}$$

x_k is the molar fraction of specie k.

All of the equations presented thus far are valid in the cathode CL and GDL. The only difference between the equations for the two domains mentioned is that there is a reaction term in equation 3.14 which is only present in the CL and not in the GDL. The equation for the source term, R_i can be found in 3.4.3 Darcy's Law for Multi—phase Flow.

It is important to note that the extended Butler—Volmer equation is used, shown in equation 2.3. Specifically, the concentration quotients were replaced by the mole fraction multiplied by the total concentration, where an example is given for water vapor. Where the only difference for hydrogen would be using the hydrogen molar fraction instead of the molar fraction for water.

$$\frac{c_{r,s}(x,y)}{c_o^*} = x_{H_2O}\frac{p}{RT} \tag{3.19}$$

p is the pressure, T is temperature and x_{H_2O} is the molar fraction of water.

Phase Transport in Porous Media

The equations for phase transport in porous media are required when taking multi—phase flow into account together with Darcy's law presented in 3.4.3 Darcy's Law for Multi—phase Flow. The equations are somewhat similar to Darcy's law however for clarity's sake, the equations for phase transport are fully presented, separately. These equations are valid in the entire geometry besides the PEM. It is also only valid in the cathode when it is assumed that liquid water is present with no water vapor, unlike when the Maxwell—Stefan equations are used.

It should be stated that unlike the VOF method where the interface between the immiscible phases is tracked, the phase transport method does not track the interface. This makes this method that was used slightly simplified. Nevertheless, with the help of the capillary pressure, the microscopic surface effects are taken into account. The equations for phase transport in porous media are presented in equations 3.20 and 3.21. However, the reaction term is only present in the CL and the

equations are valid in the entire geometry except for the PEM.

$$\nabla \cdot (\rho_i \mathbf{u}_i) = R_i \tag{3.20}$$

$$\mathbf{u}_i = -\frac{\kappa_{\mathrm{r,i}}}{\mu_i}\kappa \nabla p_i - \rho_i \mathbf{g} \tag{3.21}$$

$\kappa_{\mathrm{r,i}}$ is the relative permeability for the specie i, κ is the permeability, μ_i is the dynamic viscosity of specie i, p_i is the pressure for component i and $\mathbf{g}$ is the gravitational constant.

The pressure of specie i is defined according to equation 3.22, where p is the absolute pressure calculated with Darcy's law and p_{c} is the capillary pressure.

$$p_i = p + p_c \tag{3.22}$$

The capillary pressure is then modelled using the Leverett J—function shown in equation 3.23

$$p_c = \frac{J\gamma \cos\theta}{\sqrt{\kappa/\epsilon_p}} \tag{3.23}$$

ϵ_p is the porosity, γ is the surface tension, θ is the contact angle and lastly, J is the so—called J—function. All of the mentioned variables are constant except for the J—function, which is modelled as a function of the liquid volume fraction, s_l, as shown in equation 3.24 [Kumbur et al., 2007]. The equation used is only valid for hydrophilic media, when using a contact angle that less than 90°. However, for GDLs in electrolyzers, the hydrophobicity is relatively large. The reason an equation for the J—function for hydrophilic media was used despite the GDL being hydrophobic was due to numerical instabilities and convergence issues generated by the simulation software.

$$J = 1.417\,(1 - s_l) - 2.120\,(1 - s_l)^2 + 1.263\,(1 - s_l)^3 \tag{3.24}$$

The reaction term is modelled the same as for Darcy's law shown in equation

3.38.

The relative permeability is modelled as the square of its respective specie volume fraction, as presented in equation 3.25.

$$\kappa_{\mathrm{r,i}} = s_i^2 \tag{3.25}$$

To distinguish the expression used for the concentration quotient with phase transport from the Maxwell—Stefan equations, the volume fraction was multiplied with the total concentration instead of the molar fraction for the gas phase. When considering the liquid phase, the concentration quotient was equal to only the volume fraction of the liquid phase.

Extended Water Transport Model

The modelling techniques used for this aspect of the model were taken completely from Weber and Newman [2004a]. This model allows for calculation of the water flux through the membrane, both through electroosmotic drag but also diffusion. Equation 3.6 will become slightly more complex due to the introduction of a new variable, namely, the chemical potential of water, denoted as μ_0. The introduction of the chemical potential permits the extended model to take into account the transport of water based on concentration gradients, thus, adding more complexity and detail to the model. When using the equations presented by Weber and Newman [2004a], it was assumed that the transport was liquid—equilibrated in the anode and a derivative of the simultaneous liquid— and vapor—equilibrated transport mode when it was assumed that the water vapor is formed in the cathode. To clarify what is meant with the previous statement is that the liquid parameters were used for the conductivites and drag- and transport coefficients. However the moles of water per mole of sulfonic acid sites known as λ was computed using an expression for water vapor shown in equation 3.26, where $a_{H_2O,gas}$ is calculated using the molar fraction of water calculate with the Maxwell—Stefan equations. In addition to that, a mass source was calculated for the conversion of water in liquid phase to vapor phase, given a concentration difference between the PEM and the CL. More detailed information regarding this is presented in the latter part of this section.

$$\lambda = \begin{bmatrix} \left(-0.6\mathrm{a}_{H_2O,gas}^3 + 0.85\mathrm{a}_{H_2O,gas}^2 - 0.2\mathrm{a}_{H_2O,gas} + 0.153\right) \times (\mathrm{T} - 313) \\ +39\mathrm{a}_{H_2O,gas}^3 - 47.7\mathrm{a}_{H_2O,gas}^2 + 23.4\mathrm{a}_{H_2O,gas} + 0.117 \end{bmatrix} \tag{3.26}$$

The governing equations for the extended water transport model are presented in equations 3.27 and 3.28. Equation 3.27 is a variant of equation 3.6 and equation 3.28 is a mole balance. These equations are only valid in the CL and PEM in both the anode and the cathode.

$$j_l = -\kappa_L \nabla \Phi_l - \frac{\kappa_L \xi_L}{F} \nabla \mu_0 \tag{3.27}$$

$$N_0 = -\frac{\kappa_L \xi_L}{F} \nabla \Phi_l - \left(\alpha_L + \frac{\kappa_L \xi_L^2}{F^2}\right) \nabla \mu_0 \tag{3.28}$$

The subscript denotes that the variable is for liquid—equilibrated transport. κ_L is the electrolyte conductivity, ξ_L is the electroosmotic transport coefficient, α_L is the transport coefficient defined in equation 3.29. j_v is the volumetric current density that is obtained from the Butler—Volmer equation.

$$\alpha = -\frac{N_0}{\nabla \mu_0} \tag{3.29}$$

To put it in words, the transport coefficient is defined as the quotient of the flux of water, N_0 and the chemical potential of water, μ_o when no current is applied. The negative sign is due to the movement of water against the chemical potential gradient.

The electroosmotic coefficient is defined in equation 3.30. N_+ is the flux of protons, thus, the electroosmotic coefficient is defined as the flux of water with respect to the flux of protons.

$$\xi = \frac{N_0}{N_+} \tag{3.30}$$

The expression used for electrolyte conductivity, transport coefficient and the electroosmotic drag are presented in equation 3.31 — 3.33. The equations were

determined empirically, equation 3.31 and 3.32 were from Zenyuk et al. [2016] and equation 3.33 was from Weber and Newman [2004a]. For reasons of numerical stability, the coefficients in the equations were slightly altered from the coefficients used in the articles as shown below. Where ϵ_{m} is the volume fraction in the membrane phase and T_{t} is the triple point temperature of water.

$$\kappa_L = 50(0.39)^{1.5} \exp\left[\frac{12450}{R}\left(\frac{1}{T_t} - \frac{1}{T}\right)\right]\epsilon_m^{1.5} \tag{3.31}$$

$$\alpha_L = 8.1 \times 10^{-9}\epsilon_m^{1.5} \tag{3.32}$$

$$\xi_{\mathrm{L}} = \exp\left[\frac{1000}{R}\left(\frac{1}{T_{\mathrm{ref}}} - \frac{1}{T}\right)\right] \tag{3.33}$$

As mentioned in the beginning of this section, the method used to account for the simultaneous liquid— and vapor—equilibrated transport was a derivative of the methods presented in Weber and Newman [2004a]. In addition to the techniques mentioned, equation 3.32 was used to account for the evaporation of water based on a concentration gradient between the cathodic catalyst layer and the membrane. k_{evap} is the rate constant for condensation/evaporation taken from Zenyuk et al. [2016], $a_{H_2O,gas}$ is the activity of water inside the gas bubbles and the activity of water in the membrane, $a_{H_2O,mem}$ is modelled as equation 3.35, taken from Zenyuk et al. [2016]. Where $a_{\mathrm{H_2O,gas}} = x_{\mathrm{H_2O,c}}$ for vapor phase water in the cathode, by setting it equal to the molar fraction of water in the cathode as mentioned in the beginning of this section. Due to that water is present in liquid form in the anode, $a_{H_2O,gas}$ is set to unity.

$$N_0 = k_{evap}\left(a_{\mathrm{H_2O,gas}} - a_{\mathrm{H_2O,mem}}\right) \tag{3.34}$$

$$a_{\mathrm{H_2O,mem}} = \exp\left[\frac{(\mu_0 - \mu_{ref})}{RT}\right] \tag{3.35}$$

3.4.3 Darcy's Law for Multi—phase Flow

Given the various multi—phase flow methods presented in the background section 2.5, there were different options of methods to take the multi—phase flow into

account. VOF, mixture model and bubbly flow do not however take porous media into account and could be difficult to incorporate porous media into the equations. The scientific articles, which were stated to use these methods had larger length scales than the length scale used in this project and thus, could ignore porosity effects. Considering that, an alternative method of Darcy's law could be used, called Darcy's law for multiphase flow, shown in equation 3.37, which is coupled with equation 3.36. Darcy's law is appropriate to use in systems with small permeabilities, which is the case for an electrolyzer. The equations for Darcy's law are valid in the entire geometry besides the PEM. [Bird et al., 2007]

$$\nabla \cdot (\bar{\rho}_i \mathbf{u_i}) = Q_{\mathrm{m}} \tag{3.36}$$

$$\mathbf{u_i} = -\frac{\kappa}{\bar{\mu}}(\nabla p + \bar{\rho}\mathbf{g}) \tag{3.37}$$

$\mathbf{u_i}$ is the velocity for specie i, $\bar{\rho}$ is the mixture density, Q_{m} is the mass source, κ is the permeability, $\bar{\mu}$ is the mixture viscosity, p is the pressure and lastly, $\mathbf{g}$ is the gravitational constant. The flow is mostly governed by natural convection. This means that gravity must be taken into account as shown in the rightmost term in equation 3.37, where gravity is directed downwards in figure 3.2. A mass source is present in equation 3.36 to take into account the electrochemical reactions that take place, which is defined in equation 3.38, known as the Faraday's law of electrolysis.

$$Q_m = \frac{\nu_i j_v}{nF} M_i \tag{3.38}$$

A drag coefficient was set to three to account for the transport of protons.

Equations 3.39 and 3.40 show the expressions used to calculate the mixture viscosity and density, respectively.

$$\bar{\mu} = \frac{\bar{\rho}}{\sum_i \frac{\kappa_{rs}\rho_{s_i}}{\mu_i}} \tag{3.39}$$

$$\bar{\rho} = \sum_i s_i \rho_{s_i} \tag{3.40}$$

Where s_i represents the volume fraction of the specie i, ρ_{s_i} is the density for the specie i. Equation 3.41 shows that the Reynolds number for multi—phase flow is a lot less than one, with the width of the CL and the GDL used as the characteristic length. The fact that Reynolds number is a lot less than unity indicates that the flow is creeping flow. Which is quite expected due to that the flow in porous media oftentimes consists of a small velocity. Thus, it is reasonable to use Darcy's law for this system given the very low Reynolds number compared to Brinkman's equation or alternate forms of Darcy's law which for example use the Forchheimer term and are more appropriate within ranges of Reynolds number of 1 — 10. [Deen, 2012]

$$\mathrm{Re} = \frac{\bar{\rho} u L}{\bar{\mu}} \approx 1 \cdot 10^{-3} \tag{3.41}$$

u represents the magnitude of the velocity.

The low velocity makes it appropriate to use Darcy's law to model the fluid flow. The pressure gradient is the main driving force for Darcy's law. [Bird et al., 2007]

The Bond number presented in equation 3.42 gives a quotient between the gravitational forces and the surface tension. Using the Bond number it can be used to predict the shape of the bubbles.

$$\mathrm{Bo} = \frac{\Delta \rho g L^2}{\gamma} \tag{3.42}$$

In connection with phase transport in porous media, the form of diffusion taking place is momentum diffusion. This is due to that the diffusion of species takes place due to a pressure gradient.

3.4.4 Boundary Conditions

Table 3.1 presents the boundary conditions used in this project. The current, electrolyte potential and electrical potential were used for the electrochemical model. The mass fraction of water vapor and the mass flux were used for the Maxwell-Stefan equations. The volume fractions of oxygen and hydrogen were used in the mass

Table 3.1: Boundary conditions used in model

Variable	Boundary condition	Boundary
Electrode current, j_{s}	$-\int_{\partial\Omega}\mathbf{j}_s \cdot \mathbf{n}\mathrm{dl} = I_{cell}$	Anode BP and FC | GDL
Electrical potential, ϕ_{s}	$\phi_{\mathrm{s}} = 0[V]$	Cathode BP and FC | GDL
Electrolyte and electrical potential, i_{l} and i_{s}	$-\mathbf{n}\cdot\mathbf{i}_l = 0$ and $-\mathbf{n}\cdot\mathbf{i}_{\mathrm{s}} = 0$	Anode and cathode top and bottom boundaries of GDL, CL and PEM
Mass fraction of hydrogen gas, ω_{H_2}	$\omega_{H_2} = 0.05$	Cathode FC | GDL
Mass flux, J_{i}	$-\mathbf{n}\cdot\mathbf{J}_i = 0$	Anode and cathode PEM | CL, top and bottom boundaries of CL and GDL | BP
Pressure, p	Anode $p = 1[\mathrm{atm}]$ Cathode $p = 13[\mathrm{atm}]$	FC | GDL
Velocity vector, $\boldsymbol{u}$	$-\mathbf{n}\cdot\rho\mathbf{u} = 0$	Anode and cathode FC | GDL, top and bottom boundaries of GDL, CL and PEM, CL | PEM
Volume fraction oxygen and hydrogen, s_{i}	$s_{\mathrm{i}} = 0.08$	Anode and cathode FC | GDL
Electrical potential (Extended water transport model), ϕ_{s}	Anode $\phi_s = V_{cell}$ Cathode $\phi_{\mathrm{s}} = 0[\mathrm{V}]$	Anode and cathode BP and FC | GDL
Electrolyte potential (Extended water transport model), ϕ_{l}	$\nabla\phi_{\mathrm{l}} = 0$	GDL | CL and top and bottom of boundaries of CL and PEM
Chemical potential (Extended water transport model), μ_{l}	$\nabla\mu_{\mathrm{o}} = 0$	GDL | CL and top and bottom of boundaries of CL and PEM

balance when using a two-phase flow. The pressure and the velocity vector boundary condition were used for Darcy's law. Finally, as stated in the table, the boundary conditions for electrical potential, electrolyte potential and the chemical potential of water were used for the extended water transport model.

3.4.5 General Assumptions

Assumptions made in this project consist of:

- All gases in the simulation are treated as ideal. For a real gas to be considered as an ideal gas oftentimes the temperature needs to be high and the pressure low. This is a reasonable assumption given the compressibility factor of oxygen and hydrogen is approximately equal to that of an ideal gas at the pressures and temperatures used to in this simulation [Hoge et al., 1948].

- When the Butler—Volmer equation was used for concentration dependent kinetics, it was assumed that the kinetics had the reaction order of unity with respect to all species.

- The simulation was performed with a steady—state condition.

- Isotropic pores since all of the parameters are constant in all directions including the diffusivity, thermal conductivity and permeability.

- The simulation was performed isothermally as initial non-isothermal simulations showed that the resulting temperature gradient was small. This can be seen in figure A.1.

- The electroosmotic drag coefficient is assumed to be constant with respect to temperature, which necessarily is not the case as shown in Janssen and Overvelde [2000]. Despite the variation, it does not contribute with any large differences in the results.

- In Durst et al. [2015] and Barbir [2005] the activation energies were presented for the PEMFC reactions. It was assumed that the activation energies for the PEMEC reactions were equal to the PEMFC reactions. This assumption is difficult to motivate whether it is acceptable since in general, the PEMEC reactions are the reverse reactions taking place in the PEMFC and it is generally known that the forward rate constant is not equal to the backward rate constant because it depends on the value of the equilibrium constant. However given the lack of data available on the activation energy for the PEMEC reactions, it is assumed that the PEMEC reactions have equal activation energies as the PEMFC reactions.

3.5 Cases

There were five different cases that were considered and simulated. The cases are denoted numerically as the following:

3.5.1 Case 1 — No Flow Physics

A simulation using only the the methods presented in 3.4.1 Electrochemical Modelling. This consisted of only a charge balance, taking into no account of the flow nor the multi—phase flow, diffusion of species nor the membrane water transport. This simplified the Butler—Volmer equation as shown in equation 3.43, as there is no concentration dependent term in the equation unlike equation 2.3. A constant water content value, λ of 23 was initially run, thus, assuming that liquid water is present on both sides. In addition, a simulation with a water content of 17 in the cathode was run, assuming the presence of water vapor in the cathode.

$$j = j_0 a_v \left\{ \exp\left[\frac{\alpha_\mathrm{a} F\eta}{RT}\right] - \exp\left[-\frac{\alpha_\mathrm{c} F\eta}{RT}\right] \right\} \tag{3.43}$$

Equation 3.8 was used to calculate the ionic conductivity.

3.5.2 Case 2 — H_2O (l) fed cathode

The following case considered the multi—phase flow together with the charge balance. Thus, the methods presented in sections 3.4.1 Electrochemical Modelling, 3.4.2 Phase Transport in Porous Media and 3.4.3 Darcy's Law for Multi—phase Flow were used. For this case it is assumed that liquid water is present in both the anode and the cathode. Thus, there is no water vapor present whatsoever. For this case, the water content is set to a maximum value of 23 on both sides. Equations 3.44 and 3.45 show the Butler—Volmer equations used for the anode and cathode, respectively for this case with $s_{H_2O,a}$ being the volume fraction of water in the anode, $s_{H_2O,a}$ is the volume fraction of water in the cathode, s_{H_2} is the volume fraction of hydrogen and lastly, s_{O_2} is the volume fraction of oxygen.

$$j = j_{0,a} a_v \left\{ s_{O_2} \frac{p}{RT} \exp\left[\frac{\alpha_\mathrm{a} F\eta}{RT}\right] - s_{H_2O,a} \exp\left[-\frac{\alpha_\mathrm{c} F\eta}{RT}\right] \right\} \tag{3.44}$$

$$j = j_{0,c} a_v \left\{ s_{H_2O,c} \exp\left[\frac{\alpha_a F \eta}{RT}\right] - s_{H_2} \frac{p}{RT} \exp\left[-\frac{\alpha_c F \eta}{RT}\right] \right\} \tag{3.45}$$

Similar to the previous case, equation 3.8 was used to calculate the ionic conductivity.

3.5.3 Case 3 — Dry Hydrogen

This case is based on the fact that there is dry hydrogen in the cathode. To clarify, the water is present in the vapor phase in the cathode. This will lead to using the methods presented in 3.4.1 Electrochemical Modelling, 3.4.2 Phase Transport in Porous Media, 3.4.2 Maxwell—Stefan equations and 3.4.3 Darcy's Law for Multi—phase Flow. It is significant to note that the phase transport equations are still valid for the anode for this case. However, the main differences between this case and the previously presented case from a mathematical standpoint is that the Butler—Volmer equation is going to be slightly different in the cathode using mole fractions instead of volume fractions as presented in equation 3.46.

$$j = j_{0,c} a_v \left\{ x_{H_2O,gas} \frac{p}{RT} \exp\left[\frac{\alpha_a F \eta}{RT}\right] - x_{H_2} \frac{p}{RT} \exp\left[-\frac{\alpha_c F \eta}{RT}\right] \right\} \tag{3.46}$$

The water content, λ in the cathode is set to 17. For this case the mixture density and the mixture viscosity are calculated using mole fractions rather than volume fractions. Equation 3.8 was used for the electrolyte conductivity.

3.5.4 Case 4 — Extended Water Transport Model with Liquid Equilibration

For this case the extended water transport model was used for liquid water in the cathode thus combining the methods presented in 3.4.2 Phase Transport in Porous Media, 3.4.3 Darcy's Law for Multi—phase Flow and 3.4.2 Extended Water Transport Model.

It should be noted that equation 3.31 was used for the electrolyte conductivity. The water content was set to 23 in both the anode and the cathode. The drag coefficient that was used in the reaction equation, equation 3.38, was set to zero as the electroosmotic drag coefficient took into account for the proton transport. It is worth noting that the activity of water $a_{H_2O,gas}$ is equal to unity in equation 3.34 due it being

present as liquid form. However, $a_{H_2O,mem}$ is not unity due to that the water is bound to the membrane surface and computed in equation 3.35. For the electrolyte conductivity, σ_l was previously used, defined in equation 3.8. However, for this case, an updated electrolyte conductivity, κ_l was used, to account for the water transport in the membrane.

3.5.5 Case 5 — Extended Water Transport Model with Simultaneous Liquid Equilibration and Vapor Equilibration in the Cathode

The final case run is similar to the previous case with the only difference being that dry hydrogen was used in the cathode, making it a combination of case 3 and case 4. This one considered methods from 3.4.2 Phase Transport in Porous Media, 3.4.2 Maxwell—Stefan equations, 3.4.3 Darcy's Law for Multi—phase Flow and 3.4.2 Extended Water Transport Model. This case is identical to the previous case in the anode. The difference lies in the cathode. The difference is that the water content, λ is computed using 3.26 and thus, varying with respect to the molar fraction of water which is calculated using the Maxwell—Stefan equations.

3.6 Final Remarks

To compare the different cases to eachother, polarization curves were constructed.

The current density for the polarization curves was calculated using equation 3.47.

$$i_{\text{cell}} = \frac{-\int \sigma_s \nabla \Phi_s L_t \mathrm{dl}}{A_{cell}} \tag{3.47}$$

i_{cell} is the cell current per geometric area of the cell and A_{cell} is the cell area. The cell voltage was calculated by computing the average electrical potential, Φ_s on the boundary between the GDL and the BP and FC. Thus, this integral is computed in the mentioned boundary. L_t is the thickness of the cell.

It is worth mentioning that using the LMA, the reference exchange current densities,

$j_{0,a,ref}$ and $j_{0,c,ref}$ for the anode and cathode and the charge transfer coefficients were calibrated. The experimental data used to calibrate them originated from Liso et al. [2018].

To conclude this section, the author would like to state that the simulations performed are controlled by current for cases 1 — 3 for stability reasons. Cases 4 and 5 are controlled by voltage due to the way the model case is defined. To clarify what this means is that the boundary conditions are set to a current and the current is varied to obtain the polarization curve for a current controlled simulation and the voltage controlled simulation is set to a voltage boundary condition and the voltage is varied to obtain the polarization curve.

Chapter 4

Results and Discussion

In this section of the thesis, the results of the simulations are presented. The results consist of a comparison of the cases, a sensitivity analysis of certain parameters and lastly, model verification. Unless stated, all of the results are at $T = 80°$C.

4.1 Comparison of Cases

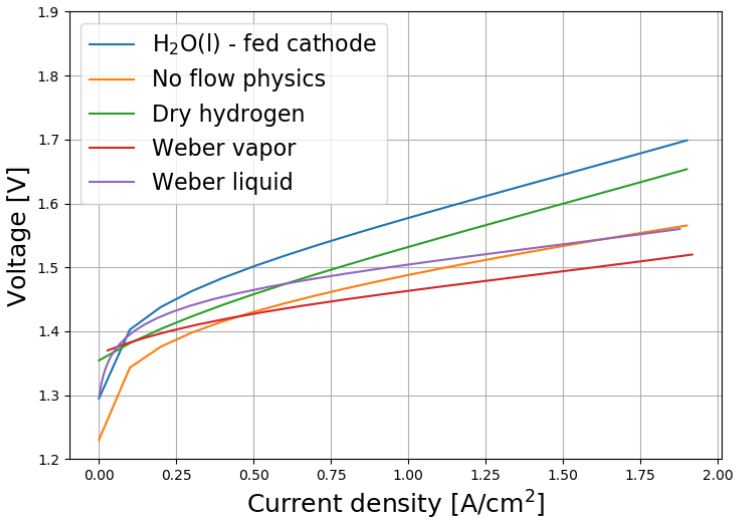

Figure 4.1: Polarization curve for the various cases at 70 ° C. No flow physics represents case 1 . H_2O (l) - fed cathode represents case 2 and dry hydrogen depicts case 3. Weber liquid represents case 4 and Weber vapor represents case 5.

There were clear differences between most of the cases in figures 4.1 and 4.2. The figures in general show larger losses at larger temperatures, given the steep polarization curves in figure 4.2.

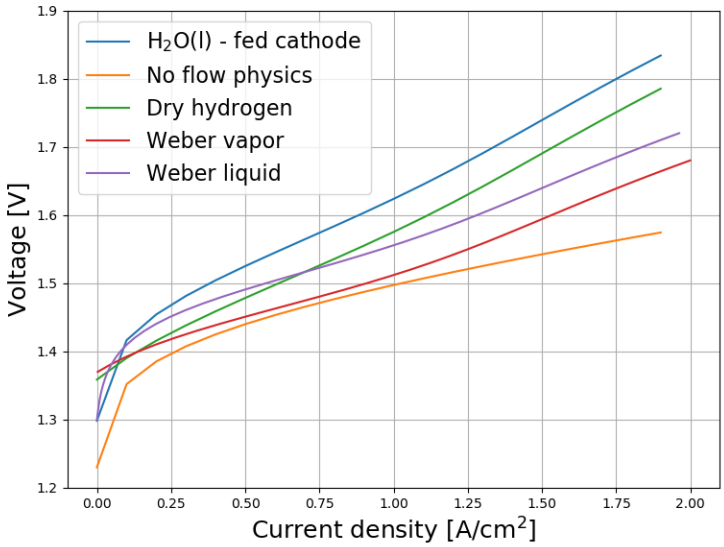

Figure 4.2: Polarization curve for the various cases at 80 ° C. No flow physics represents case 1 . H_2O (l) - fed cathode represents case 2 and dry hydrogen depicts case 3. Weber liquid corresponds to case 4 and Weber vapor corresponds to case 5.

No flow physics shows little to no difference between the two temperatures. The expression used in equations 3.8 and 3.13 are the main equations affecting the appearance of the polarization curve. Table 4.1 shows the values of the electrolyte conductivity and exchange current densities at the two temperatures. As it can be seen from the table, very little change occurs for the electrolyte conductivity and the cathodic exchange current density. However, the anodic current density does vary significantly, resulting in a 48% decrease in the exchange current density. The larger variation for the anodic exchange current density compared to the cathodic exchange current density is due to that the activation energy for the anodic electrochemical reactions is almost approximately fourfold the activation energy for the cathodic electrochemical reactions used in equation 3.13. Given the very little variations in the relevant parameters with respect to temperature, the polarization curve for *No flow physics* does not vary much either.

For the remaining cases it is quite evident that there is a much larger contribution from mass transfer to the polarization curve at the larger temperature. Diffusion increases with respect to temperature, which supports figures 4.1 and 4.2. For the four other cases, diffusion was present in many other forms such as Maxwell—Stefan diffusion for the *Dry hydrogen* case in the cathode, momentum diffusion in both the anode and the cathode for the *H_2O (l) — fed cathode* case due to the pressure

Table 4.1: The electrolyte conductivity, anodic exchange current density and cathodic current density at different temperatures

Temperature [° C]	**Electrolyte conductivity[S/m]**	**Anodic exchange current density [A/m^2]**	**Cathodic exchange current density [A/m^2]**
70	1.923	183.0	0.026
80	2.135	95.05	0.022

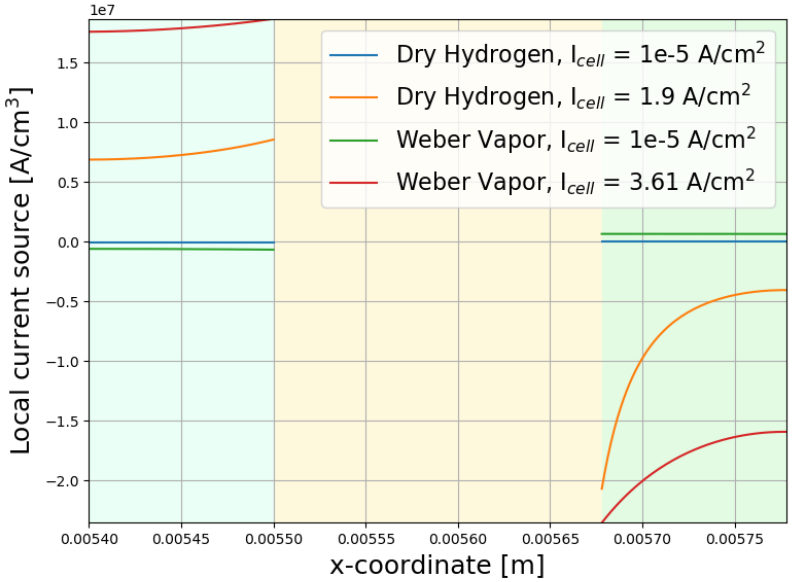

Figure 4.3: The local current source as a function of the position. The 1-dimensional plot is across the middle of the geometry. The light blue region represent the anode CL, the light green region is the nafion membrane and lastly, the yellow region is the cathode CL

gradients. For the extended water transport model, Fickian diffusion takes place. It is quite visible that the phase in which water is present in has an effect. The connection it has to the polarization curve is that the water content is affected, which in turn affects the electrolyte conductivity.

Figure 4.3 shows the current density source term. This is calculated with the Butler—Volmer equation presented in equation 2.3. The current density production is analogous to the reaction rate. Thus, the larger the current density production magnitude, the larger the rate of reaction. A gradient in the figure is quite evident for larger overpotentials. Regarding the cathode, the magnitude of the current density is the largest closest to the membrane, motivating the fine mesh near this boundary. It

is apparent that case 5, *Weber vapor* has a larger gradient for the current density distribution than for case 3, *Dry hydrogen* This is due to the large value for κ_{L} calculated in equation 3.31 compared to σ_{l} calculated in equation 3.8. κ_{L} is used for the extended water transport model as a replacement for σ_{l} to take into account the liquid—equilibrated transport. κ_{L} is approximately 20 times larger than σ_l, yielding the much more uniform current density distribution for case 5.

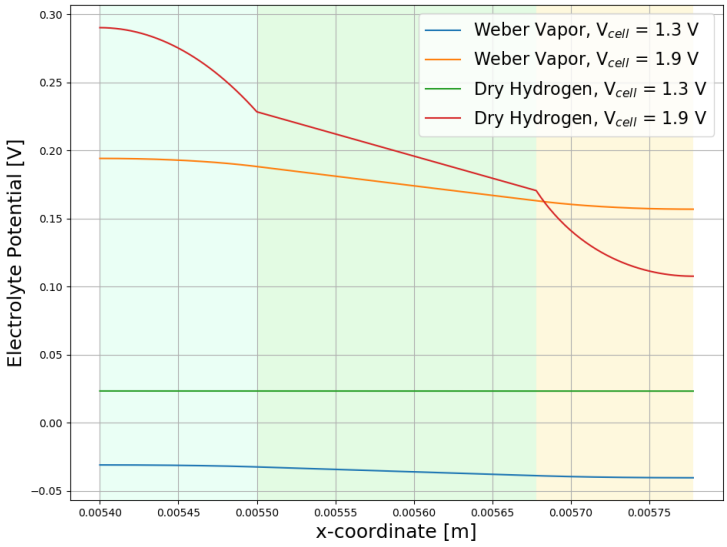

Figure 4.4: The electrolyte potential for case 3 and case 5. The light blue region represent the anode CL, the light green region is the nafion membrane and lastly, the yellow region is the cathode CL

Figure 4.4 shows how the electrolyte potential varies for two cases, case 3, *Dry hydrogen* and case 5, *Extended water transport model with simultaneous liquid equilibration and vapor equilibration in the cathode*. Interestingly, three of the curves are completely or approximately linear. The only curve that is not linear is for case 3 at $V_{\mathrm{cell}} = 1.9$ V. The reason why the two cases at $V_{cell} = 1.3$ V are practically linear is due to that the overpotential is so low so that the electrolyte potential can practically remain linear. At larger overpotentials as in the simulations ran at $V_{cell} = 1.9$ V there are other factors to take into account. As figure 4.5 shows, the electrolyte conductivity for case 5, κ_{L} is constant, while the electrolyte conductivity for case 5, σ_l is not constant along the x–coordinate. This is due to that σ_l is a function of λ, the water content, while that is not true for κ_L. Since for cases 3 and 5, water is present as vapor form, λ is 17 and λ in the membrane is computed using a linear function depending on its value in the GDL. Regarding the electrolyte potential, when

the anode and cathode electrolyte conductivity is not equal to eachother, it will lead to a non—linear behaviour in each respective side, which is the case in figure 4.4.

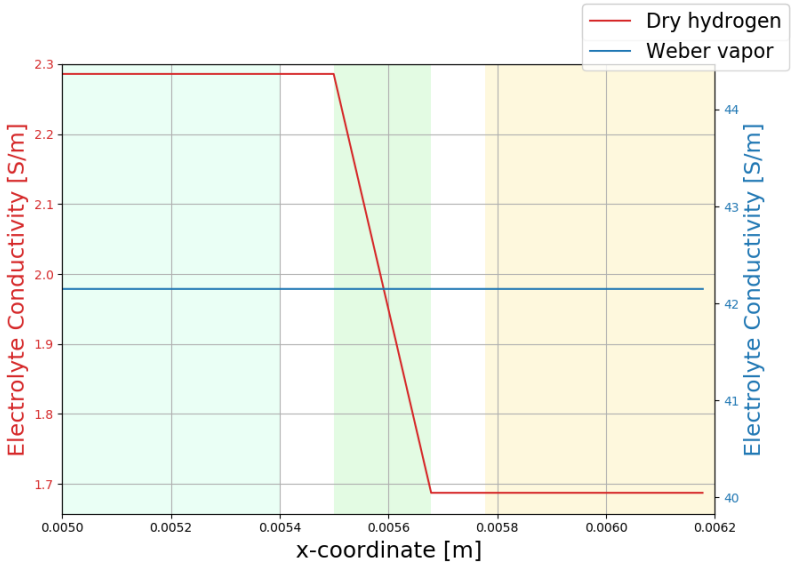

Figure 4.5: The electrolyte conductivity in the middle of the geometry as a function of the x—coordinate. The light blue region represents the GDL in the anode, the white region is the CL, the green region is the nafion membrane and the yellow region outlines the cathode GDL.

4.2 Sensitivity Analysis

In this section of the thesis, the sensitivity analysis is presented. The parameters were halved, doubled and compared to the original parameter as the figures below present. For the sensitivity analysis the appearance of the polarization curves were compared in figure 4.6. Subfigures 4.6a — 4.6d were computed for case 1, *No flow physics* and subfigures 4.6e — 4.6f were computed for case 3, *Dry hydrogen*.

To clarify, in figures 4.6a and 4.6d the *reference* exchange current density was varied, which appears in the Arrhenius equation, equation 3.13 to calculate the *actual* exchange current density at temperature, T, giving a linear relationship between the exchange current density and its reference. Interestingly, the reference current density had a larger effect on the polarization curve in the cathode compared to the anode. For the cathodic reference exchange current density, the activation loss ceases to increase at a larger voltage for a smaller reference exchange current density due to that the cell voltage is logarithmically-inversely proportional to the current density production for activation polarization as shown in equation 4.1. j is the current

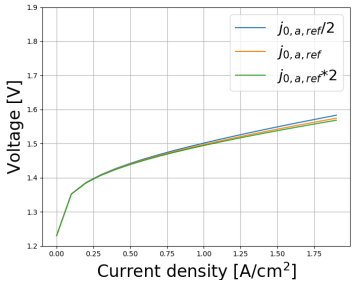

(a) The anodic exchange reference current density with a baseline case of $j_{0,a,ref} = 6008$ A/m^2

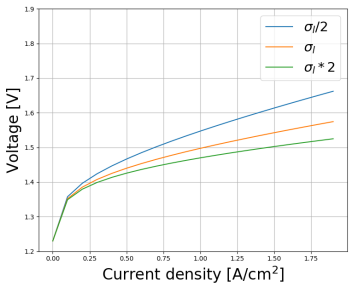

(b) The electrolyte conductivity with a baseline of $\sigma_l = 1.92$ S/m

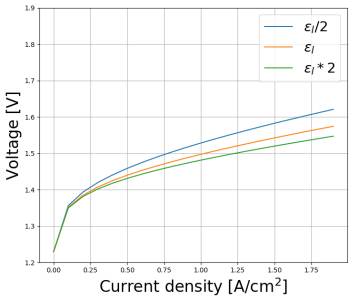

(c) The electrolyte volume fraction with a baseline of $\epsilon_l = 0.4$

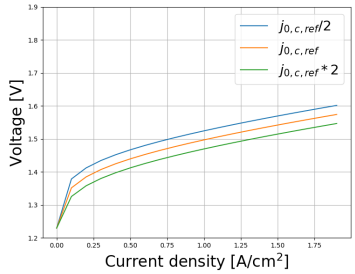

(d) The cathodic exchange reference current density with a baseline case of $j_{0,c,ref} = 0.06017$ A/m^2

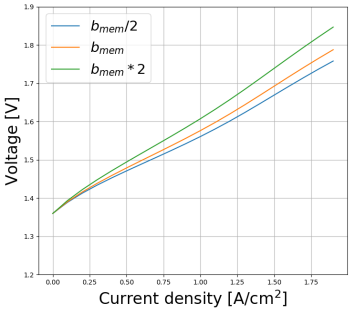

(e) The membrane thickness with a baseline of $b_{mem} = 1.78 \cdot 10^{-4}$m

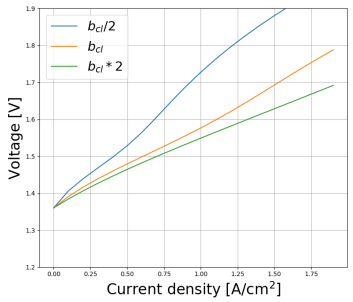

(f) The catalyst layer thickness with a baseline of $b_{mem} = 1.0 \cdot 10^{-4}$m

Figure 4.6: Sensitivity analysis for various parameters comparing the appearance of the polarization curve.

density and n is the number of electrons involved in the electrochemical reactions. A similarity between the polarization curve for the anode and the cathode was that doubling the reference exchange current density lead to a decrease in the loss and halving the exchange current density lead to an increase in the voltage loss.

$$V_{Act} = \frac{RT}{n\alpha F} \ln\left(\frac{j}{j_0}\right) \tag{4.1}$$

Equation 4.1 is the Tafel equation, which is actually only valid if one electrode at a time is studied and the overpotential is large. Nevertheless, it should not be an issue to use the equation and draw conclusions from it.

Figure 4.6b shows that similar to the reference exchange current density a smaller electrolyte conductivity yields a larger voltage loss. This is due to that the electrolyte conductivity is inversely proportional to voltage for ohmic losses, thus, giving a larger

gradient for the linear region of the polarization curve as shown in Ohm's law in equation 4.2. Where R is the resistance, I is the current and b is the material thickness.

$$V_{Ohm} = RI = \frac{b}{\sigma_l} i \tag{4.2}$$

Equation 4.2 is only valid if the ohmic loss is greatest in the membrane compared to the other regions of the PEMEC. Both equation 4.1 and 4.2 are assumed to be valid for ideal and simplified systems however qualitatively, the polarization curves obtained from the simulations should behave in the same manner.

For figure 4.6c, where the electrolyte volume fraction is varied, it has a similar motivation for the appearance of the polarization curve as for the electrolyte conductivity. As the Bruggeman relation shown in equation 3.11 was used to compute the effective electrolyte conductivity as a function of electrolyte volume fraction, ϵ_l. The electrolyte volume fraction also affected the gradient of the ohmic loss.

Figure 4.6e shows a sensitivity analysis for the membrane thickness. It shows that increasing the membrane thickness will lead to a larger voltage loss. A larger membrane thickness will give a larger ohmic loss as is viewed by the larger gradient for the larger membrane thicknesses in the figure. When the electrolyte volume fraction is doubled, there is a greater mass transfer region almost invisible in the baseline and in the halved electrolyte volume fraction.

In figure 4.6f, the catalyst layer thickness is varied. It is very evident that there is a large mass transfer loss when the thickness is doubled. There is a slight mass transfer loss that is slightly visible in the baseline. Figure 4.6f shows that

4.3 Model Verification

In this section of this thesis, certain model properties are presented and discussed.

Figure 4.7 shows how the water activity varied in its various phases for case 5. Starting with the anode, the activity of water, $a_{H_2O,gas}$ was set to unity, thus, supplies a reason for its appearance in the figure. In the cathode, $a_{H_2O,gas}$ was set equal to the molar fraction of water that is solved in the Maxwell—Stefan equations. Despite the

fact that it looks constant in figure 4.7, it is not completely constant. There is a very small gradient. The reason it is this small is due to that the main losses come from the activation polarization and the ohmic loss as presented in the polarization curve in figure 4.2. In the CLs and the PEM, the activity of the membrane bounded water varies. It was calculated using equation 3.35, which explains the exponential shape of the curves. In figure 4.8, it is clear that the chemical potential varies exponentially similar to the activity. The gradient in chemical potential is the driving force for the diffusion of water in the membrane phase, thus, giving its shape in figure 4.7. To sum it up, the larger the gradient of the chemical potential, the larger the activity gradient.

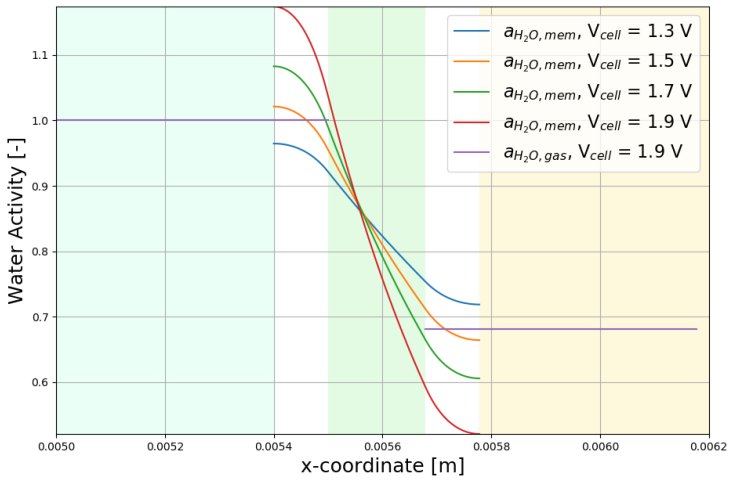

Figure 4.7: The activity of water for case 5. The different regions are represented by the different colors. The light blue region represents the GDL in the anode, the white region is the CL, the green region is the nafion membrane and the yellow region outlines the cathode GDL.

The dependent variables from the extended water transport models are presented in figure 4.8 for case 5. The chemical potential as mentioned in the previous paragraph varies exponentially similar to the electrolyte potential. The water transport is larger at larger voltages due to a greater chemical potential. One thing worth mentioning regarding the electrolyte potential is that the increase in the activity gradient at larger voltages, gives an increase in the ion transport across the membrane. Due to that the results for the electrolyte potential were covered in 4.1 Comparison of Cases, the reader is referred to that section for more information.

The vector field in figure 4.9 shows the volumetric flux of water as well as its

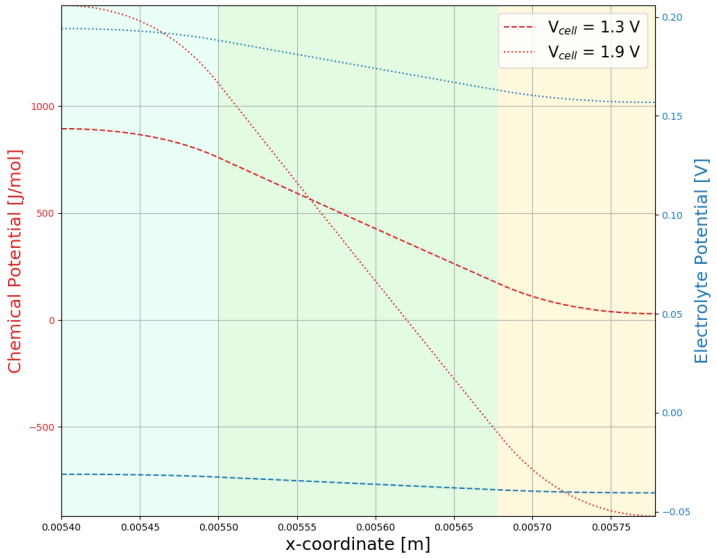

Figure 4.8: This figure shows the chemical potential and the electrolyte potential in the same plot. The light blue region represent the anode CL, the light green region is the nafion membrane and lastly, the yellow region is the cathode CL

magnitude for case 2, with the size of the vector representing the magnitude. Given the boundary conditions set for Darcy's law for multi—phase flow, the fluid flows upwards against gravity and exits through the gas channel. A clearer snapshot is shown in figure 4.10a, illustrating the flux in the middle portion of the cathode. Interestingly, there is some backflow present in the top region of the cathode shown clearly in figure 4.10b. With the way the model is currently set up, the electrolytic cell is not used to its best efficiency with the backflow, leading to undesired flow properties. The backflow moves upwards rather than downwards due to the fluid that is already moving upwards from the lower parts of the cathode shown in figure 4.9. With the backflow moving upwards, there is a slight accumulation in the top right corner.

Figure 4.11 shows that there is not much of a variation in the volume fraction of the liquid phase, s_l. In the lower parts of the anode, there is a slight gradient in the volume fraction. The fact that the volume fraction does not vary much indicates that the diffusion of reactants is faster than the rate of reaction, resulting in the lack of a volume fraction gradient.

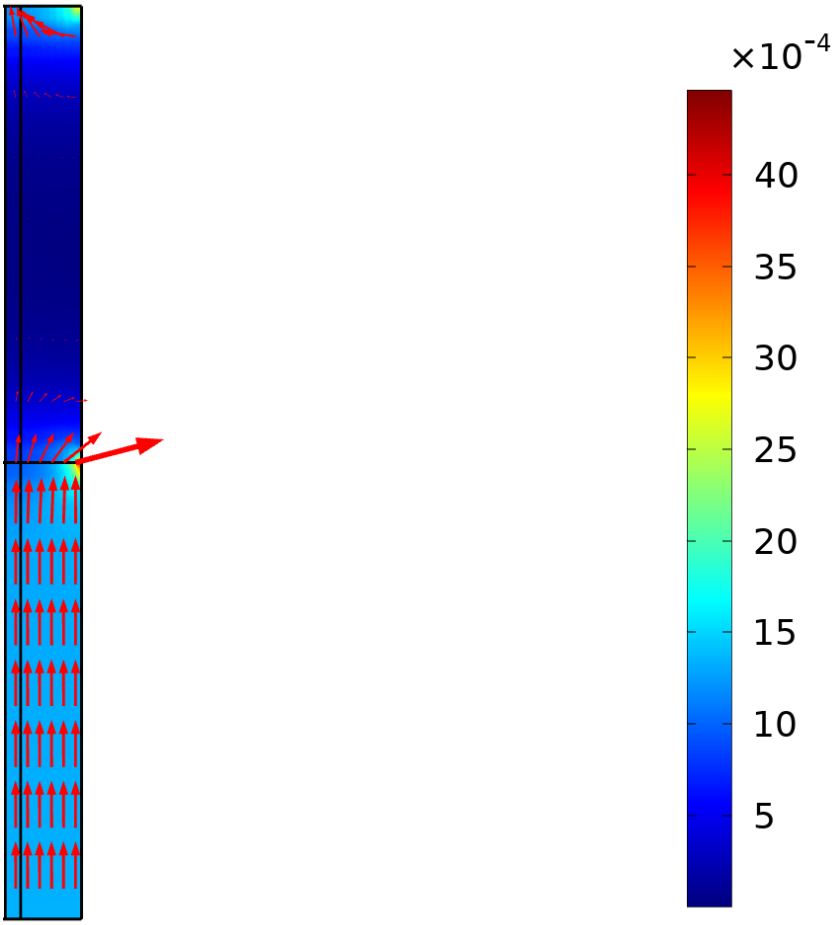

Figure 4.9: Vector field of the water volumetric flux at $V_{cell} = 1.9$ V in the cathode for case 2 with the units m/s

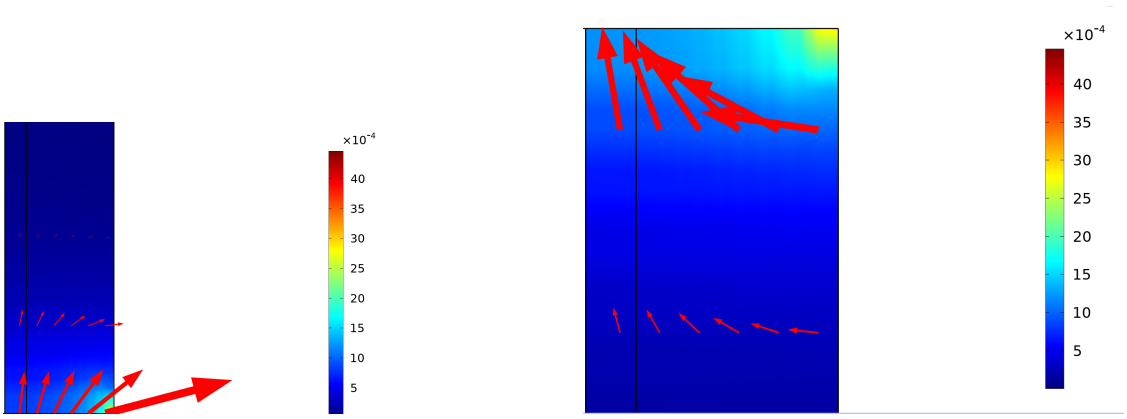

(a) Middle region of cathode

(b) Top region of cathode

Figure 4.10: A zoomed in shapshot of figure 4.9

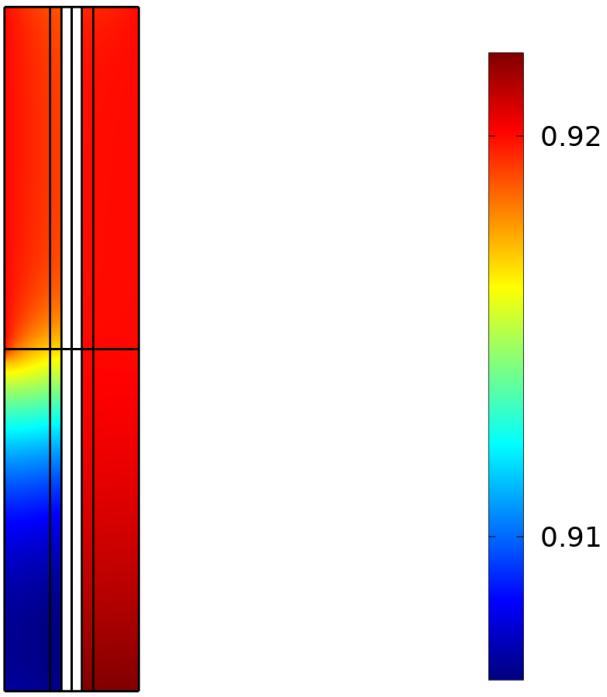

Figure 4.11: The liquid volume fraction for case 2 at $V_{cell} = 1.9$ V

Chapter 5

Conclusion

5.1 Limitations

The model cannot compute the capillary pressure correctly due to the faulty J—function. When using the correct expression for the J—function along with a contact angle which exceeds 90°, the model has difficulty converging. This shows a weakness within the model, leading to an incorrect value of the capillary pressure. The contact angle that was supposed to be used would give a negative capillary pressure. In addition, equation 5.1 shows the Bond number of the anode and the cathode, since there was not a large difference between the anode and the cathode Bond number. The fact that the number is larger than one indicates that the gravitational force will dominate over the surface tension. This will imply that the shape of the bubbles will be less spherical and more ovoidal [Nguyen et al., 2013].

$$\mathrm{Bo} \approx 4.15 \tag{5.1}$$

Due to the hydrophobic media in the GDL and the large Bond number, it would clearly indicate a contact angle larger than 90° is required to be used.

Additionally, there is not a vast amount of experimental data for electrolyzers available due to a lack of research. This causes the model verification to be difficult leading to a slight lack in confidence for the results.

5.2 Future Work

Regarding the model used for this thesis, it could be extended to a three—dimensional model. An extension would permit analysis of an additional axis, yielding more results and different phenomena to analyze and study. On the contrary, an extension would lead to a longer simulation time, depending on the complexity of the geometry and the fineness of the mesh. It also increases the risk of numerical instability since there are more factors that need to be taken into account.

The extended water transport model that was used for the final cases, has been validated in Weber and Newman [2004b]. However, it was validated for a fuel cell model and has yet to the author's knowledge been validated for electrolyzers. The expressions used for the parameters were mainly extracted from Weber and Newman [2004a] and Zenyuk et al. [2016]. Calibrated expressions would possibly have yielded in more reliable results. The next step would be to validate the extended water transport model in an electrolyzer model by using experimental data, whereas the simulation results can be used from this thesis.

5.3 Final Words

The aim of this thesis was to study the governing physics of the PEMEC by considering the different phenomena that exist, by varying parameters to determine if they have a large effect on the model and lastly, to determine which assumptions would have a large impact on the model by looking at the five different cases.

In summary, as the results showed, taking into account various phenomena, the polarization curves looked different depending on the assumptions made, with generally more losses at a higher temperature. Using solely electrochemical modelling techniques many of the losses taking place in a polarization curve could be captured similar to the other cases. The phase in which water is present in from cases 2—5 also has an effect on the appearance of the polarization curve due to its effect on the electrolyte conductivity.

As explained in 2.2 Related Work, one of the first PEMEC models ever was created as late as in 2002. Implying that this is a fairly new field of research. There is a vast amount of work left to be accomplished within the field of electrolyzer modelling.

Among them include for example more models for practical usage of large scale electrolyzers, more models using multi-phase modelling and more experimental work indicate that there is a lot of room for research!

Nomenclature

α_a	Charge transfer coefficient, anode [-]
α_c	Charge transfer coefficient, cathode [-]
α_L	Transport coefficient for liquid—equilibrated transport [mol/(J cm s)]
α_V	Transport coefficient for vapor—equilibrated transport [mol/(J cm s)]
$\bar{\mu}$	Viscosity of mixture [Pa s]
$\bar{\rho}$	Density of mixture [kg/m^3]
$\bar{V}_o$	Molar volume of water [m^3/mol]
$\boldsymbol{g}$	Gravitational acceleration constant [m/s^2]
$\boldsymbol{u}$	Velocity vector [m/s]
ϵ_l	Electrolyte volume fraction [-]
$\epsilon_m^{1.5}$	Volume fraction of the membrane phase [-]
ϵ_p	Porosity [-]
ϵ_s	Electrode volume fraction [-]
η	Overpotential [V]
η_{Act}	Activation overpotential [V]
η_{Diff}	Diffusion overpotential [V]
η_{Ohm}	Ohmic overpotential [V]

γ	Surface tension to infiltrate and expand channel [N/m]
$_{s}$	Electrical potential on the surface [A/m^2]
κ	Permeability [m^2]
κ_{L}	Electrolyte conductivity for liquid—equilibrated transport [S/cm]
$\kappa_{r,i}$	Relative permeability [-]
κ_{V}	Electrolyte conductivity for vapor—equilibrated transport [S/cm]
λ	Moles of water per mole of sulfonic acid sites (water content) [-]
μ	Dynamic viscosity [Pa s]
μ_{o}	Chemical potential of water [J/mol]
ν_{i}	Reaction coefficient [-]
ω_{i}	Mass fraction of specie i [A]
ϕ	Basis function [-]
ϕ_{i}	Volume fraction of of specie i [-]
Φ_{l}	Electrolyte potential [V]
Φ_{s}	Electrical potential on the surface [A/m^2]
ϕ_{s}	Electrical potential [V]
ρ	Density [kg/m^3]
$\sigma_{l,eff}$	Effective ionic conductivity [S/m]
σ_{l}	Ionic conductivity [S/m]
$\sigma_{s,eff}$	Effective electrical conductivity [S/m]
σ_{s}	Electrical conductivity [S/m]
θ	Contact angle of water on Nafion [deg]

$\tilde{D}_{\mathrm{i,k}}$ Effective diffusivity [m^2/s]

ξ_{L} Electroosmotic coefficient for liquid—equilibrated transport [-]

ξ_{V} Electroosmotic coefficient for vapor—equilibrated transport [-]

$a_{\mathrm{H_2O,gas}}$ Activity of water inside gas bubbles [-]

a_{v} Specific catalyst surface area [1/m]

a_{j} Scaling factor in FEM [-]

a_0 Activity of water [-]

a_{H_2O} Activity of water in the membrane [-]

B Number of mesh elements [-]

b Material thickness [m]

c_{o}^* Reference concentration [mol/m^3]

$c_{\mathrm{o,s}}(x, y)$ Surface concentration on the side where oxidation occurs [mol/m^3]

$c_{\mathrm{r,s}}(x, y)$ Surface concentration on the side where reduction occurs [mol/m^3]

d_{o} Diffusional driving force that acts on specie, k [1/m]

$D_{\mathrm{i,\,k}}$ Diffusion coefficient of specie i in k [m^2/s]

E Electrode potential [V]

e Residual [-]

E_{eq} Equilibrium electrode potential [V]

E_{OCV} Open circuit voltage [V]

E_a Activation energy [J/mol]

F Faraday's constant [C/mol]

I Current [A]

I_{cell} Cell current [A/m^3]

I_{cell} Cell current density per geometric area [A/m^2]

i_{cell} Current density per area of cell [A/m^2]

$i_{v,tot}$ Total current source [A/m^3]

j Current density[A/m^2]

$j_{\text{o,a}}$ Anodic exchange current density [A/m^2]

$j_{\text{o,c}}$ Cathodic exchange current density [A/m^2]

j_{o} Exchange current density [A/m^2]

J_{i} Flux of specie i [kg/(m^2 s)]

j_{s} Electrode current on the surface [A/m^2]

j_{s} Normal vector [-]

j_{s} Solid phase current density [A/m^2]

j_{v} Current density from electrochemical reactions[A/m^3]

$j_{0,a,ref}$ Reference anodic exchange current density at the reference temperature[A/m^2]

$j_{0,c,ref}$ Reference cathodic exchange current density at the reference temperature[A/m^2]

$j_{0,ref}$ Reference exchange current density at the reference temperature[A/m^2]

k_{evap} Rate constant for evaporation/condensation of water [g mol/(J cm^2 s)]

L Characteristic length [m]

M Number of domain equations [-]

M_i Molar mass of specie i [g/mol]

N_{+} Flux of protons [mol/(m^2 s)]

N_+ Superficial flux density of protons [mol/cm^2 s]

N_o Superficial flux density of water [mol/cm^2 s]

N_0 Flux of water [mol/(m^2 s)]

n_e Number of electrons in an electrochemical reaction [-]

P Order of basis [-]

p Pressure [Pa]

$p_{c,k}$ Critical pressure of specie k [atm]

p_L Liquid pressure [Pa]

p_A Absolute pressure [Pa]

p_c Capillary pressure [Pa]

Q_l Electrolyte current source term [A/m^3]

Q_s General current source term [A/m^3]

Q_m Mass source [kg/(m^{3}s)]

R Resistance [Ω]

R Universal gas constant [J/(K mol)]

r Channel radius [m]

S Fraction of channels expanded [-]

s Problem size (number of variables) [-]

s_l Liquid volume fraction [-]

T Temperature [K]

$T_{c,k}$ Critical temperature of specie k [K]

T_{ref} Reference temperature [K]

T_{t} Triple-point temperature of water [K]

u Abolute value of the velocity [m/s]

$V(r)$ Normalized differential volume of channels of radius [m^3]

V_{cell} Cell voltage [V]

Y Number of dimensions [-]

x_{k} Molar fraction of specie k [-]

Bo Bond number [-]

Re Reynold's number [-]

Chapter 6

Bibliography

S.S. Kumar and V. Himabundu. Hydrogen production by PEM water electrolysis – A review. *Materials Science for Energy Technologies*, 2019. doi: 10.1016/j.mset.2019.03.002. URL https://doi.org/10.1016/j.mset.2019.03.002.

L. Jones P. Atkins and L. Laverman. *Chemical Principles*. W.H. Freeman, 7 edition, 2016. ISBN 9781464183959.

A.C Olesen and S.K. Kær. The Effect of PFSA Membrane Compression on the Predicted Performance of a High Pressure PEM Electrolysis Cell. *Journal of The Electrochemical Society*, 2015. doi: 10.1149/06803.0099ecst. URL https://doi.org/10.1149/06803.0099ecst.

C.Y. Biaku, N.V. Dale, M.D. Mann, H. Salehfar, A.J. Peters, and T. Han. A semiempirical study of the temperature dependence of the anode charge transfer coefficient of a 6 kW PEM electrolyzer. *Journal of Hydrogen Energy*, 2008. doi: 10.1016/j.ijhydene.2008.06.006. URL https://doi.org/10.1016/j.ijhydene.2008.06.006.

K. Onda, T.Murakami, T. Hikosaka, and M. Kobayashi. Performance analysis of polymer-electrolyte water electrolysis cell at a small-unit test cell and performance prediction of large stacked cell. *Journal of Electrochemical Society*, 2002. doi: 10.1149/1.1492287. URL https://doi.org/10.1149/1.1492287.

B. Han, S. M Steen, J. Mo, and F.Y. Zhang. Electrochemical performance modeling of a proton exchange membrane electrolyzer cell for hydrogen energy. *Internation*

Journal of Hydrogen Energy, 2015. doi: 10.1016/j.ijhydene.2015.03.164. URL http://dx.doi.org/10.1016/j.ijhydene.2015.03.164.

H. Kim, M. Park, and K.S. Lee. One-dimensional dynamic modeling of a high pressure water electrolysis system for hydrogen production. *Internation Journal of Hydrogen Energy*, 2012. doi: 10.1016/j.ijhydene.2012.12.006. URL http://dx.doi.org/10.1016/j.ijhydene.2012.12.006.

S. Toghyani, E. Afshari, and E. Baniasadi. Three-dimensional computational fluid dynamics modeling of proton exchange membrane electrolyzer with new flow field pattern. *Journal of Thermal Analysis and Calorimetry*, 2018. doi: 10.1007/s10973-018-7236-5. URL https://doi.org/10.1007/s10973-018-7236-5.

Jianhu Nie, Yitung Chen, Steve Cohen, Blake D. Carter, and Robert F. Boehm. Numerical and experimental study of three-dimensional fluid flow in the bipolar plate of a PEM electrolysis cell. *International Journal of Thermal Sciences*, 2009. doi: 10.1016/j.ijthermalsci.2009.02.017. URL http://dx.doi.org/10.1016/j.ijthermalsci.2009.02.017.

S. Touré, A. Konaté, D. Traoré, and D Fofana. Novel determination method of charge transfer coefficient of PEM fuel cell using the Lagrange's multiplier method. 2018. doi: 10.1088/1755-1315/188/1/012041. URL https://doi.org/10.1088/1755-1315/188/1/012041.

A. Z. Weber and J. Newman. Transport in polymer-electrolyte membranes: Ii. mathematical model. *Journal of The Electrochemical Society*, 2004a. doi: 10.1149/1.1639157. URL https://iopscience.iop.org/article/10.1149/1.1639157.

A.Z. Weber and J. Newman. Transport in Polymer-Electrolyte Membranes : III. Model Validation in a Simple Fuel-Cell Model. *Journal of The Electrochemical Society*, 2004b. doi: 10.1149/1.1639158. URL https://doi.org/10.1149/1.1639158.

Saeed Sadeghi Lafmejani, Anders Christian Olesen, and Søren Knudsen Kær. VOF modelling of gaseliquid flow in PEM water electrolysis cell micro-channels. *Journal of Hydrogen Energy*, 2017. doi: 10.1016/j.ijhydene.2017.05.079. URL http://dx.doi.org/10.1016/j.ijhydene.2017.05.079.

Zhiqiang Niu, Kui Jiao, and Fan Zhang. Direct numerical simulation of two-phase turbulent flow in fuel cell flow channel. *Journal of Hydrogen Energy*, 2015. doi: 10.1016/j.ijhydene.2015.11.026. URL http://dx.doi.org/10.1016/j.ijhydene.2015.11.026.

J. Nie and Y. Chen. Numerical modeling of three-dimensional two-phase gas–liquid flow in the flow field plate of a PEM electrolysis cell . *Journal of The Electrochemical Society*, 2009. doi: 10.1016/j.ijhydene.2010.01.050. URL https://doi.org/10.1016/j.ijhydene.2010.01.050.

T. Berning, M. Odgaard, and S. K. Kær. A Computational Analysis of Multiphase Flow Through PEMFC Cathode Porous Media Using the Multifluid Approach. *Journal of The Electrochemical Society*, 2009. doi: 10.1149/1.3206691. URL https://doi.org/10.1149/1.3206691.

S.Z. Hosseini Larimi, A.Ramiar, and Q. Esmaili. The effect of inlet velocity of water on the two-phase flow regime in the porous transport layer of polymer electrolyte membrane electrolyzer . *International Journal of Heat and Mass Transfer*, 2018. doi: 10.1007/s00231-018-2436-x. URL https://doi.org/10.1007/s00231-018-2436-x.

W.M. Deen. *Analaysis of Transport Phenomena*. Oxford University Press, 2012. ISBN 9780199740253.

H. K. Versteeg and W. Malalasekera. *An Introduction to Computational Fluid Dynamics: The Finite Volume Method*. Pearson Education, 2007. ISBN 978-0-13-127498-3.

B. Nilsson. Applied transport phenomena, the finite element method. 2018.

N. Ottosen and H. Petersson. *Introduction to the Finite Element Method*. Pearson Education, 1992. ISBN 9780134738772.

T. A. Zawodzinski and S. Gottesfeld. Polymer Electrolyte Fuel Cell Model. *Journal of The Electrochemical Society*, 1991. doi: 10.1149/1.2085971. URL https://doi.org/10.1149/1.2085971.

J. Durst, C. Simon, F. Hasché, and H. A. Gasteiger. Hydrogen Oxidation and Evolution Reaction Kinetics on Carbon Supported Pt, Ir, Rh, and Pd

Electrocatalysts in Acidic Media. *Journal of The Electrochemical Society*, 2015. doi: 10.1149/2.0981501jes. URL https://doi.org/10.1149/2.0981501jes.

F. Barbir. *PEM Fuel Cells: Theory and Practice*. Elsevier, 2005. ISBN 9780123877109.

R. B. Bird, W. E. Stewart, and E. N. Lightfoot. *Transport Phenomena*. John Wiley & Sons, Inc., 2 edition, 2007. ISBN 978-0-470-11539-8.

J. C. Slattery R. B. Bird. Calculation of the diffusion coefficient of dilute gases and of the self diffusion coefficient of dense gases. *AlChE Journal*, 1958. doi: 10.1002/aic.690040205. URL https://doi.org/10.1002/aic.690040205.

E. C. Kumbur, K. V. Sharp, and M. M. Mench. Validated Leverett Approach for Multiphase Flow in PEFC Diffusion Media: I. Hydrophobicity Effect. *Journal of The Electrochemical Society*, 2007. doi: 10.1149/1.2784283. URL https://doi.org/10.1149/1.2784283.

I. V. Zenyuk, P. K. Das, and A. Z. Weber. Understanding Impacts of Catalyst-Layer Thickness on Fuel-Cell Performance via Mathematical Modeling. *Journal of Electrochemical Society*, 2016. doi: 10.1149/2.1161607jes. URL https://doi.org/10.1149/2.1161607jes.

Harold J. Hoge, Cyril H. Meyers, and Robert E. McCoskey. Charts of Compressibility Factors and Charts Showing Quantities Delivered by Commercial Cylinders for Hydrogen, Nitrogen, and Oxygen. 1948. URL https://www.govinfo.gov/content/pkg/GOVPUB-C13-84f8d22fa812849b3066386db90cef50/pdf/GOVPUB-C13-84f8d22fa812849b3066386db90cef50.pdf.

G.J.M. Janssen and M.L.J. Overvelde. Water transport in the proton-exchange-membrane fuel cell:measurements of the effective drag coefficient. *Journal of Power Sources*, 2000. doi: 10.1016/S0378-7753(01)00708-X. URL https://doi.org/10.1016/S0378-7753(01)00708-X.

V. Liso, G. Savoia, S. S. Araya, G. Cinti, and S. K. Kær. Modelling and Experimental Analysis of a Polymer Electrolyte Membrane Water Electrolysis Cell at Different Operating Temperatures. *Energies*, 2018. doi: 10.3390/en11123273. URL https://doi.org/10.3390/en11123273.

C. T. Nguyen, H. M. Gonnermann, Y. Chen, C. Huber, A. A. Maiorano, A. Gouldstone, and J. Dufek. Film drainage and the lifetime of bubbles. *Geochemistry, Geophysics, Geosystems*, 2013. doi: 10.1002/ggge.20198. URL https://doi.org/10.1002/ggge.20198.

G. J. M. Janssen. A Phenomenological Model of Water Transport in a Proton Exchange Membrane Fuel Cell. *Journal of The Electrochemical Society*, 2001. doi: 10.1149/1.1415031. URL https://doi.org/10.1149/1.1415031.

Thomas A.Zawodzinski, John Davey, and Shimshon Gottesfeld. The water content dependence of electro-osmotic drag in proton-conducting polymer electrolytes. *Electrochimica Acta*, 1995. doi: 10.1016/0013-4686(94)00277-8. URL https://doi.org/10.1016/0013-4686(94)00277-8.

M. F. Kaya and N. Demir. Numerical Investigation of PEM Water Electrolysis Performance for Different Oxygen Evolution Electrocatalysts. *Fuel Cells From Fundamentals To Systems*, 2018. doi: 10.1002/fuce.201600216. URL https://doi.org/10.1002/fuce.201600216.

Appendix A

Additional Results

Table A.1: The calibrated parameters presented together with their calibrated values

Parameter	**Value**
Cathodic charge transfer coefficient for the anode, $\alpha_{\text{an,c}}$	0.8942
Anodic charge transfer coefficient for the cathode, $\alpha_{\text{cat,a}}$	0.76846
Reference anodic exchange current density, $i_{0,a,ref}$	6008[A/m^2]
Reference cathodic exchange current density, $i_{0,c,ref}$	0.06017[A/m^2]

The electrolyte potential was also calibrated using the experimental data from Liso et al. [2018]. However since the electrolyte potential is not constant, the calibrated expression is presented in 3.8.

The relationship between the two charge transfer coefficients are shown in equations A.1 and A.2.

$$\alpha_{\text{an,c}} = 1 - \alpha_{\text{an,a}} \tag{A.1}$$

$$\alpha_{\text{cat,c}} = 1 - \alpha_{\text{cat,a}} \tag{A.2}$$

Figure A.1 was obtained by simulating with temperature dependence.

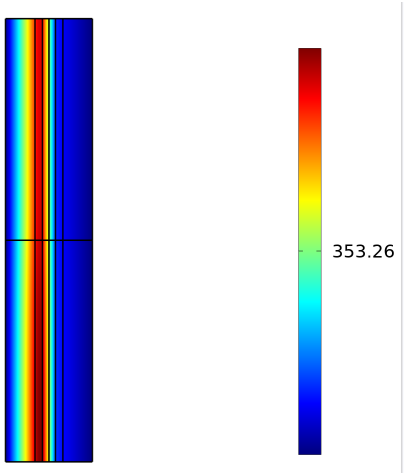

Figure A.1: Temperature profile at $V_{cell} = 1.9\,\mathrm{V}$

Appendix B

Extended Water Transport Model

$$j_v = S\left(-\kappa_L \nabla \Phi_l - \frac{\kappa_L \xi_L}{F}\bar{V}_0 \nabla p_{\mathrm{L}}\right) + (1-S)\left(-\kappa_{\mathrm{V}} \nabla \Phi_l - \frac{\kappa_{\mathrm{V}} \xi_{\mathrm{V}}}{F}\nabla \mu_0\right) \tag{B.1}$$

$$N_0 = S\left[-\frac{\kappa_L \xi_L}{F}\nabla \Phi_l - \left(\alpha_L + \frac{\kappa_L \xi_L^2}{F^2}\right)\bar{V}_0 \nabla p_{\mathrm{L}}\right] + (1-S)\left[-\frac{\kappa_{\mathrm{V}} \xi_{\mathrm{V}}}{F}\nabla \Phi - \left(\alpha_{\mathrm{V}} + \frac{\kappa_{\mathrm{V}} \xi_{\mathrm{V}}^2}{F^2}\right)\nabla \mu_0\right] \tag{B.2}$$

The variables that contain the subscript L represent the liquid water transport and the variables containing the subscript V regard the vapor phase for water. κ is the electrolyte conductivity, ξ is the electroosmotic drag coefficient and α is the transport coefficient. These variables are described more in detail in section 3.4.2 Extended Water Transport Model. μ_0 is the chemical potential and $\bar{V}_0$ is the molar volume of water.

S is defined as the fraction of channels expanded, which corresponds to a saturation, thus, if the transport is completely vapor—equilibrated there are no expanded channels and hence, $S = 0$. $S = 1$ for a full liquid—equilibrated transport.

For vapor—equilibrated transport, the chemical potential of water is shown in equation B.3. This equation divides the chemical potential into two separate driving forces, namely, activity and pressure driving forces. In Weber and Newman [2004a], it is stated that the pressure driving force is often expressed in terms of activity using Henry's law. In Janssen [2001], equation B.3 was not used to divide the two driving forces, instead the chemical potential was used directly in the governing equations, namely, equations B.1 and B.2.

$$\nabla \mu_0 = RT \nabla \ln a_0 + \bar{V}_0 \nabla p \tag{B.3}$$

For liquid—equilibrated transport, equation B.3 simplifies to equation B.4. With the absence of any vapor phase in the membrane, the liquid pressure is modelled as a function of the physical properties of the membrane due to the absence of gas. θ is the contact angle, which represents the average surface energy interactions between the water and the channel, which is somewhat hydrophobic for a liquid—equilibrated membrane. This value is a constant and it has been measured for water on Nafion's surface [A.Zawodzinski et al., 1995]. The channel radius, r, can be determined using equation B.5.

$$\nabla \mu_0 = \overline{V_0} \nabla p_{\mathrm{L}} \tag{B.4}$$

$$V(r) = \frac{1}{0.3 r \sqrt{2\pi}} \exp\left[-\frac{1}{2} \left(\frac{\ln r - \ln(1.25)}{0.3} \right)^2 \right] \tag{B.5}$$

Where $\overline{V_0}$ is the molar volume, which is the quotient of density and molar mass. For liquid—equilibrated transport the leftmost term on the RHS is not included due to that the activity is unity.

The pressure is modelled according to equation B.6,

$$p_{\mathrm{L}} = -\frac{2\gamma \cos\theta}{r} \tag{B.6}$$

Appendix C

Parameters

Table C.1: The values used for the geometry parameters and their source

Parameter	**Value**	**Source**
Membrane thickness, b_{mem}	0.178 mm	[Kaya and Demir, 2018]
Catalyst layer thickness, b_{CL}	0.1 mm	[Kaya and Demir, 2018]
Catalyst layer thickness, b_{GDL}	0.4 mm	[Kaya and Demir, 2018]
Cell height, H_{cell}	5 mm	[Kaya and Demir, 2018]
Cell area A_{cell}	2.98 cm^2	[Liso et al., 2018]

Table C.2: The values used for the electrochemical parameters

Parameter	**Value**	-
Active specific surface area , A_{v}	$1 \cdot 10^6 1/\text{m}$	-
Electrical conductivity, σ_{s}	530 S m^{-1}	-
Electrode volume fraction, ϵ_s	0.4	-
Electrolyte volume fraction, ϵ_l	0.4	-
Anodic activation energy, E_a	66 kJ/mol	[Durst et al., 2015]
Cathodic activation energy, E_c	16 kJ/mol	[Barbir, 2005]

Table C.3: Parameters used for species transport, Darcy's law for multi—phase flow and the extended water transport mdoel

Parameter	**Value**	**Source**
Rate constant for evaporation/condensation of water, k_{evap}	7.27 mol/(m^2 s)	[Zenyuk et al., 2016]
Permeability, K	$1 \cdot 10^{-11}$m^2	-
Membrane volume fraction, ϵ_{M}	1	-
Contact angle, θ	57.8°	-
Porosity ϵ	0.4	

Appendix D

Material properties

Equation D.1 was used to calculate the the viscosity of liquid water as a function of temperature.

$$\mu_{H_2O,l} = 1.3799566804 - 0.0212240191 51T + 1.3604562827 \cdot 10^{-4}T^2 - 4.6454090319 \cdot 10^{-7} T^3 + 8.9042735735 \cdot 10^{10}T^4 - 9.079069268610^{13} \cdot T5 + 3.845733148810^{16} \cdot T^6 \tag{D.1}$$

Equation D.2 was used to calculate the density of liquid water as a function of temperature.

$$\rho_{H_2O,l} = 0.000010335053319 \cdot T^3 - 0.013395065634452 \cdot T^2 + 4.969288832655160 \cdot T +432.257114008512 \tag{D.2}$$

Equation D.3 was used to calculate the viscosity of water vapor as a function of temperature.

$$\mu_{H_2O,v} = -1.42022867 \cdot 10^{-6} + 3.8345571 \cdot 10^{-8} \cdot T + 3.85222958 \cdot 10^{-12} \cdot T^2 + 2.1019569 \cdot 10^{-15} \cdot T^3 \tag{D.3}$$

Equation D.4 was used to calculate the density of water vapor as a function of temperature and absolute pressure, p_A.

$$\rho_{H_2O,v} = \frac{0.01802 p_A}{RT} \tag{D.4}$$

Equation D.5 was used to calculate the viscosity of oxygen as a function of temperature.

$$\mu_{O_2} = -5.55818182 \cdot 10^{-7} + 9.24202797 \cdot 10^{-8} \cdot T - 8.71841492 \cdot 10^{-11} \cdot T^2 + 4.82983683 \cdot 10^{-14} \cdot T^3 \tag{D.5}$$

Equation D.6 was used to compute the density of oxygen as a function of temperature and absolute pressure.

$$\rho_{O_2} = \frac{0.032 p_A}{RT} \tag{D.6}$$

Equation D.7 was used to compute the viscosity of hydrogen as a function of temperature.

$$\mu_{H_2} = 2.14524642 \cdot 10^{-6} + 2.54245 \cdot 10^{-8} \cdot T - 1.0235587 \cdot 10^{-11} \cdot T^2 + 2.80895021 \cdot 10^{-15} \cdot T^3 \tag{D.7}$$

Equation D.8 was used to compute the density of hydrogen as a function of temperature and absolute pressure.

$$\rho_{O_2} = \frac{0.002016 p_A}{RT} \tag{D.8}$$